Viscoelastic Love numbers and long-period geophysical effects

A Michel, Jean-Paul Boy

Geophysical Journal International

Geophys. J. Int. (2022) **228,** 1191–1212
Advance Access publication 2021 September 13
GJI Gravity, Geodesy and Tides

https://doi.org/10.1093/gji/ggab369

Viscoelastic Love numbers and long-period geophysical effects

A. Michel and J.-P. Boy

ITES (UMR 7063), EOST/Université de Strasbourg, CNRS, ENGEES, 5 rue René Descartes, 67084 *Strasbourg cedex, France. E-mail: alexandre.michel@unistra.fr*

Accepted 2021 September 10. Received 2021 September 7; in original form 2021 January 14

SUMMARY

Long term deformations strongly depend on the earth model and its rheological parameters, and in particular its viscosity. We give the general theory and the numerical scheme to compute them for any spherically non-rotating isotropic earth model with linear rheology, either elastic or viscoelastic. Although the Laplace transform (LT) is classically used to compute viscoelastic deformation, we choose here instead, to implement the integration with the Fourier transform (FT) in order to take advantage of the fast FT algorithm and avoid some of the LT mathematical difficulties. We describe the methodology to calculate deformations induced by several geophysical signals regardless of whether they are periodic or not, especially by choosing an adapted time sampling for the FT. As examples, we investigate the sensitivity of the displacements due to long period solid Earth tides, glacial isostatic adjustment and present-day ice melting, to anelastic parameters of the mantle. We find that the effects of anelasticity are important for long period deformation and relatively low values of viscosities for both Maxwell and Burgers models. We show that slight modifications in the rheological models could significantly change the amplitude of deformation but also affect the spatial and temporal pattern of the signal to a lesser extent. Especially, we highlight the importance of the mantle anelasticity in the low degrees deformation due to present-day ice melting and encourage its inclusion in future models.

Key words: Elasticity and anelasticity; Fourier analysis; Loading of the Earth; Tides and planetary waves; Satellite gravity.

1 INTRODUCTION

The deformation of the Earth or other planets induced by surface loading processes or tidal forces have been largely studied through the formalism first developed by Love (1911) for spherically symmetric non-rotating elastic isotropic (SNREI) bodies. Dimensionless numbers called Love numbers characterize the perturbation applied on the body and its interior rheological parameters. Among the different Love numbers, tidal Love numbers (TLN) are computed for an external potential perturbation and are especially used for tidal forces. In the other hand, load Love numbers (LLN) are computed for mass load laid on the body surface and are mainly used for external circulation of oceanic, hydrological and atmospheric masses. Several tools have already been developed to compute elastic Love numbers (Martens *et al*. 2019) and anelastic Love numbers (Spada 2008; Kachuck & Cathles 2019) using, respectively, the historical normal modes approach (Peltier 1974; Vermeersen & Sabadini 1997) and the propagator approach (Sabadini *et al*. 1982).

The main sources of deformation observed by the different geodetic measurements are the solid Earth tides (Agnew 2015) and ocean tidal loading (Carrere *et al*. 2016; Martens *et al*. 2016a) reaching, respectively, an amplitude of 30 and 10 cm. The circulation of global geophysical fluids induces continuous loading deformations from daily and subdaily periods, to seasonal cycles (Argus *et al*. 2014a, 2017) and longer period such as the postglacial rebound (Peltier *et al*. 1981).

Solid Earth tides and ocean tidal loading are usually modelled using the IERS (International Earth Rotation and Reference Systems Service) conventions (Petit & Luzum 2010) which provide the different Love numbers to be used. Those Love numbers vary not only with the harmonic degree, but also with the order, to include the Earth's ellipticity and rotation. The anelasticity is taken into account at long periods based on the absorption band process classically used in seismology (Dehant & Zschau 1989; Benjamin *et al*. 2006) which may be not appropriate for the very long periods timescales (beyond Chandler wobble period), compared to a consistent viscoelastic model with Maxwell or Burgers rheologies.

Several long time geophysical signals suggest to take into account the anelasticity of the mantle to explain the observed displacement rates (Caron *et al*. 2017). The most common example is the glacial isostatic adjustment (GIA, Spada *et al*. 2011; Argus *et al*. 2014b;

Peltier *et al*. 2015). However, some other signals such as Earth tides (especially the Moon's node of 18.6 yr period) or present-day ice melting (Spada *et al*. 2012; Luthcke *et al*. 2013), could also be affected by viscoelastic rheologies. In most studies (Zhang *et al*. 2019; Li *et al*. 2020), the anelasticity of the Earth's response to surface loading processes, including present-day ice mass loss, is still neglected but should be considered to provide a unique consistent frame of study within other long period loading deformation signals such as GIA (Métivier *et al*. 2020).

To compute viscoelastic deformations, we use the correspondence principle which allows to search solution of the gravito-elastic system in the frequency domain, using the Laplace or Fourier transforms of the time dependent variables. Most of studies use the Laplace transform (LT) which allows to handle perturbations with finite or infinite temporal extensions (Peltier 1974; Spada 2008; Sabadini *et al*. 2016). To avoid the mathematical difficulties of the LT related to the residues integration using normal modes approach (Tanaka *et al*. 2006; Spada & Boschi 2006), another option is to use the Fourier transform (FT) which is much more suitable for numerical computation thanks to algorithms such as fast-Fourier transform (FFT). The mathematical issue using the last one is that FT resolution theoretically only works with periodic signals (which have an infinite temporal extension) such as tides but not *a priori* with deformations generated by singular events such as post-seismic deformations (PSD), or secular signals such as GIA and ice melting. Dealing with finite temporal signal could create apodization phenomena which can affect the nature of the FT. In this study, we show that all the issues related to the FT including aliasing and apodization, can be overpassed with appropriate resampling of non-periodic geophysical signals.

The aim of the paper is to revisit the computation of surface deformations due to various geophysical effects, for example solid Earth tides, GIA and present-day ice mass loss, with a special attention paid to the Earth's Mantle anelasticity, using a consistent rheology model. In Section 2, we describe the different rheological models used in this study, for example elastic, and the anelastic Maxwell and Burgers rheology and provide Hooke's law in the time and frequency domain. We present the integration of the system and its variant for viscoelastic case, respectively, in Sections 3, 3.3 and 5 is devoted to the investigation of the anelastic rheology on displacements for three classical long period examples: solid Earth tides, GIA and present-day ice mass loss. Discussion and concluding remarks are finally given in Section 6.

2 RHEOLOGICAL MODELS

2.1 Elastic rheology

Hooke's law for an elastic medium and its equivalent for an isotropic viscous fluid are given by the stress–strain relations

$$\begin{cases} \sigma = \lambda^e \mathrm{Tr}(\varepsilon)\mathbf{I} + 2\mu^e \varepsilon \\ \sigma = \chi \mathrm{Tr}(\dot{\varepsilon})\mathbf{I} + 2\eta\dot{\varepsilon} \end{cases}, \tag{1}$$

where σ is the stress tensor, ε is the strain tensor, (λ^e, μ^e) are the Lamé elastic coefficients, η and χ are, respectively, the first and second viscosity, Tr() is the trace of the tensor, $\mathbf{I}$ the identity tensor and we note with upper dot the derivative with time. The second viscosity χ is related to the volume viscosity which is zero for an incompressible medium. Considering the difficulty of measuring χ experimentally, it is very common to neglect it in dense media like a fluid or a solid (which is the usual Stokes hypothesis), and to consider the medium as Newtonian (Ranalli 1995). We will adopt this hypothesis in the following, in which the second equation of eq. (1) is limited to its second term.

It is convenient to separate the compressible and incompressible part of each equation and solve both independently. We write each tensor (generic notation τ is used) as the direct sum of a full trace $\overline{\tau} = 1/3\mathrm{Tr}(\tau)\mathbf{I}$ and a null trace $\tau' = \tau - 1/3\mathrm{Tr}(\tau)\mathbf{I}$ tensor. The tensor $\overline{\varepsilon}$ represents an homogeneous and isotropic compression of the material—equivalent to an hydrostatic pressure—while ε' contains the remaining shear deformation. Applying this decomposition in the elastic equation of eq. (1), we obtain

$$\begin{cases} \overline{\sigma} = (3\lambda^e + 2\mu^e)\overline{\varepsilon} \;=\; 3K\overline{\varepsilon} \\ \sigma' = 2\mu^e \varepsilon' \end{cases}, \tag{2}$$

where K is the bulk modulus. This decomposition provides to the user the possibility to choose independently the compressible and the incompressible models as parts of a global rheological model.

2.2 Maxwell rheology

Spada (2008) provides a complete synthesis of several viscoelastic models. The most used and widely studied viscoelastic model for the Earth mantle is Maxwell rheology (Peltier 1974; Wu & Peltier 1982; Vermeersen *et al*. 1996; Spada 2013). A Maxwell material is modelled by the association of a spring and a damper in series (Fig. 1). It behaves then like an elastic medium for short timescale and like a viscous fluid for long timescale. The elastic part is compressible of moduli λ^e and μ^e, and the viscous part is incompressible (see Section 2.1) of viscosity η^m. The compressible relation is then directly given by eq. (2) : $\overline{\sigma} = (3\lambda^e + 2\mu^e)\overline{\varepsilon}$, while the incompressible part is given by the differential equation

$$\frac{\dot{\sigma}'}{2\mu^e} + \frac{\sigma'}{2\eta^m} = \dot{\varepsilon}'. \tag{3}$$

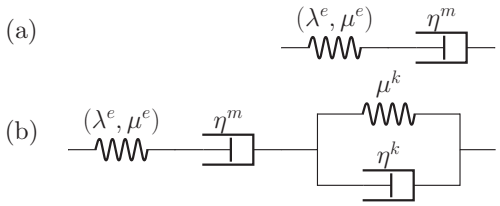

Figure 1. Maxwell (a) and Burgers (b) rheological models with a compressible elastic modulus λ^e.

We choose to find solutions of this equation in the Fourier domain, using the FT $\widetilde{\sigma}'(\omega)$ and $\widetilde{\varepsilon}'(\omega)$ of, respectively, σ' and ε', where $\omega = 2\pi f$ is the angular frequency. The differential equation (eq. 3) then becomes

$$\widetilde{\sigma}' = 2\mu^e \left[1 - \frac{1}{\left(\mathrm{i}\omega \dfrac{\eta^m}{\mu^e} + 1 \right)} \right] \widetilde{\varepsilon}' = 2\mu^e \left[1 - m(\omega) \right] \widetilde{\varepsilon}'. \tag{4}$$

The supplementary term $m(\omega)$ induced by the presence of the damper is characteristic of a first order low-pass system of cut-off frequency $\omega^{em} = \mu^e/\eta^m$. The total stress vanishes if either ω or η^m tends to 0, but the system is elastic ($m(\omega) = 0$) if η^m tends to infinity.

2.3 Burgers rheology

In order to introduce further relaxation timescales, we can associate an incompressible Kelvin model in series with the Maxwell block in a global model known as Burgers model (Fig. 1). We note, respectively, μ^k and η^k the shear and viscous moduli of the Kelvin part. Since the Kelvin block is incompressible, the compressible equation is reduced to its elastic part as in Section 2.2. The differential equation of the incompressible part is now a second-order equation:

$$\frac{\ddot{\sigma}'}{2\mu^e\mu^k} + \dot{\sigma}' \left(\frac{1}{2\mu^k\eta^m} + \frac{1}{2\mu^k\eta^k} + \frac{1}{2\mu^e\eta^k} \right) + \frac{\sigma'}{2\eta^m\eta^k} = \frac{\ddot{\varepsilon}'}{\mu^k} + \frac{\dot{\varepsilon}'}{\eta^k}. \tag{5}$$

This equation is quite general and we can recover several simpler models by taking the limit cases when parameters tends to infinity. Taking η^k or μ^k infinite, reproduces the Maxwell model (the Kelvin part is then equivalent to a wire transmitting all the stress but not the strain). Taking η^m infinite reproduces the general Kelvin model (SLS-V in Spada 2008) while additionally taking μ^e infinite returns the simple Kelvin model. Finally, we find the elastic limit behaviour with $\eta^k, \eta^m \longrightarrow +\infty$ or $\mu^k, \eta^m \longrightarrow +\infty$.

Again as a linear rheology, the solution in the Fourier domain gives a linear relation between the FT of stress and strain

$$\widetilde{\sigma}' = 2\mu^e \frac{\omega^2 - \mathrm{i}\omega\omega^{kk}}{\omega^2 - \mathrm{i}\omega\left(\omega^{em} + \omega^{ek} + \omega^{kk}\right) - \omega_r^2} \widetilde{\varepsilon}', \tag{6}$$

where $\omega^{ij} = \mu^i/\eta^j$ and e, m and k means, respectively, elastic, Maxwell and Kelvin moduli. We also define the resonant frequency $\omega_r = \sqrt{\omega^{em}\omega^{kk}}$. Removing the pure elastic part from this equation, it also returns the expression of a low-pass filter but of order two, with several characteristic timescales. First, we find the Maxwell frequency ω^{em} which establishes the intersection between the low and high frequencies characteristic behaviours. A second order system can also resonates if the excitation is close to the resonant frequency ω_r and the quality factor is large. If the second condition is not satisfied (which is the case for reasonable values of parameters) the system is no longer resonant. Then, from the high frequency asymptotic straight line the Bode diagram reaches a first plateau in medium frequencies before reaching later its final horizontal asymptote at low frequencies. The length of the intermediate plateau and the shape of the diagram between it and the low frequencies asymptote is controlled, respectively, by the frequency ω^{kk} and the frequency ω^{ek}. As the Kelvin viscosity increases, the intermediate plateau shrinks and we tend to a pure Maxwell response.

The eq. (6) can be rewritten as the product of the Maxwell term defined in eq. (4) and an additional contribution due to the addition of the Kelvin modulus:

$$\widetilde{\sigma}' = 2\mu^e \left[1 - m(\omega) \right] \left[\frac{1}{1 + b(\omega)} \right] \widetilde{\varepsilon}', \tag{7}$$

with

$$b(\omega) = \frac{\mathrm{i}\omega\omega^{ek}}{(\mathrm{i}\omega + \omega^{kk})(\mathrm{i}\omega + \omega^{em})}. \tag{8}$$

The eq. (7) is very convenient to numerically implement the stress function depending if we consider either elastic [$b(\omega) = 0$; $m(\omega) = 0$], Maxwell [$b(\omega) = 0$] or Burgers rheologies which are the most commons used models in the literature.

Table 1. Summary of the different viscoelastic models developed in this article with an elastic compressible part. We also computed the equivalent frequency-dependent Lamé parameters for each model.

Rheological model	Elastic	Maxwell	Burgers
Frequential relation (incompressible part)	$\widetilde{\sigma}' = 2\mu^e\widetilde{\varepsilon}'$	$\widetilde{\sigma}' = 2\mu^e\,[1 - m(\omega)]\,\widetilde{\varepsilon}'$	$\widetilde{\sigma}' = 2\mu^e\,[1 - m(\omega)]\left[\dfrac{1}{1 + b(\omega)}\right]\widetilde{\varepsilon}'$
Specific function definition	–	$m(\omega) = \dfrac{1}{(\mathrm{i}\omega/\omega^{em} + 1)}$	$b(\omega) = \dfrac{\mathrm{i}\omega\omega^{ek}}{(\mathrm{i}\omega + \omega^{kk})\,(\mathrm{i}\omega + \omega^{em})}$
$\lambda(\omega)$	λ^e	$\lambda^e + \dfrac{2}{3}\mu^e m(\omega)$	$\lambda^e + \dfrac{2}{3}\mu^e\left[\dfrac{m(\omega) + b(\omega)}{1 + b(\omega)}\right]$
$\mu(\omega)$	μ^e	$\mu^e[1 - m(\omega)]$	$\mu^e\,[1 - m(\omega)]\left[\dfrac{1}{1 + b(\omega)}\right]$

2.4 Generalized Hooke's law

The combination of the two linear solutions of the differential equations (compressible and incompressible part) in the Fourier domain, gives the general stress–strain expression. This general solution can be written as a Hooke's law with new frequential functions $\lambda(\omega)$ and $\mu(\omega)$ defined such that

$$\widetilde{\sigma} = \lambda(\omega)\mathrm{Tr}(\widetilde{\varepsilon})\mathbf{I} + 2\mu(\omega)\widetilde{\varepsilon}. \tag{9}$$

For any linear time-dependent rheological model we can use the above expression in the frequency domain instead of the usual Hooke's law (eq. 1) used for an elastic medium. This is known as the correspondence principle firstly mentioned in Lee (1955) and Lee *et al*. (1959) with the LT. We use here the FT which is numerically easier to deal with but has an a priori more restricted area of applications (Tobie *et al*. 2005). Nevertheless, we show later that the calculation of time Love numbers derived from LT like in Spada (2008) or Kachuck & Cathles (2019) is not necessary for usual geophysical cases. Those can be treated in the Fourier domain with a special attention given to the sampling and the numerical computation of FT. The Table 1 gives the equivalent functions $m(\omega)$, $b(\omega)$, $\lambda(\omega)$ and $\mu(\omega)$ for elastic, Maxwell and Burgers compressible models in order to use the correspondence principle in viscoelastic earth models.

3 LOVE NUMBERS COMPUTATION

3.1 Self gravitating elastic system

Either elastic or generalized Hooke's law, completes the gravito-elastic deformation system of equation already including the Poisson equation, the mass conservation and the momentum conservation. The solution of displacement and perturbed potential produced by a small perturbation can be calculated for an spherically symmetric non-rotating elastic isotropic (SNREI) Earth considering a decomposition in spherical harmonics (SH). The resulting system widely known as y_{in} system (Alterman *et al*. 1959; Longman 1962) contains 6 spheroidal independent equations in radial and tangential displacement (y_{1n}, y_{3n}), radial and tangential traction vector components (y_{2n}, y_{4n}), on potential (y_{5n}) and modified gravity function (y_{6n}). For stratified earth models with a liquid core like preliminary reference earth model (PREM, Dziewonski & Anderson 1981) or STW105 also known as reference earth model (REF, Kustowski *et al*. 2008), the density ρ_0 and the rheological parameters λ and μ depends on r which require to perform the integration numerically. Several studies already dealt with the inclusion of a liquid core by taking the limit of the equations with no shear ($\mu \to 0$). This led to the Longman paradox fully explained and solved in Chinnery (1975) for a stratified liquid core. We use its results to propagate our solution throughout the liquid core.

The y_{in} system can be solved applying boundary conditions at the centre (null displacements and potential) and at the surface. The latter conditions are dependent of the perturbation as fully explained by Hinderer & Legros (1989). For the general case, if we note P an external pressure, ζ a surface mass load, U an external potential and τ a tangential component of traction we can write the general boundary conditions for a given nth degree

$$\begin{cases} y_{2n}(a) = -g_e\zeta_n - P_n \\ y_{4n}(a) = \tau_n \\ y_{6n}(a) + \dfrac{n+1}{a}y_5(a) = \dfrac{2n+1}{a}U_n + 4\pi\mathcal{G}\zeta_n \end{cases}, \tag{10}$$

where g_e is the norm of surface gravity. Farrell (1972) and Longman (1962) already showed that the surface mass load could also be written as an external potential U' such that $\zeta_n = (2n+1)/4\pi\mathcal{G}aU'_n$. The complete resolution scheme is reported in the Appendix.

3.2 Love numbers definition

It is commonly accepted to give the solution of the displacement and the perturbed potential at the Earth surface in function of the perturbation potential (U_n or U'_n) and dimensionless numbers first introduced by Love (1911) depending on the earth model and its rheological behaviour.

Table 2. Tidal Love numbers (TLN) (h_n, l_n, k_n) definition for an external potential perturbation U and load Love numbers (LLN) (h'_n, l'_n, k'_n) definition for an equivalent surface mass load potential U'.

	External potential	Surface loading
$\begin{bmatrix} y_{1n}(a) \\ y_{3n}(a) \\ y_{5n}(a) \end{bmatrix} =$	$U_n \begin{bmatrix} h_n/g_0(a) \\ l_n/g_0(a) \\ (1+k_n) \end{bmatrix}$,	$U'_n \begin{bmatrix} h'_n/g_0(a) \\ l'_n/g_0(a) \\ (1+k'_n) \end{bmatrix}$

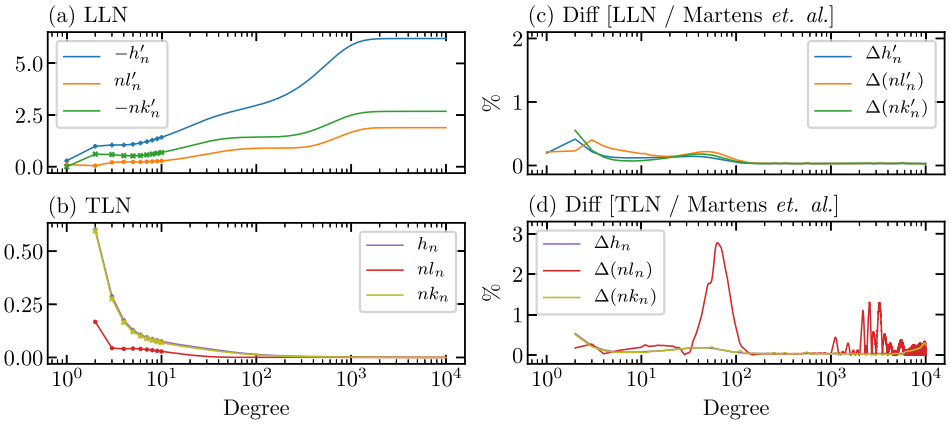

Figure 2. LLN (a) and TLN (b) for PREM with a liquid core obtained with presented integration scheme. Panels (c) and (d) are, respectively, the difference of LLN and TLN with those calculated with *LoadDef* program from Martens *et al*. (2019).

Love numbers are the response of a system to a unit perturbation potential and are then very convenient to compare solutions from different earth models. We will only use in the following, the TLN corresponding to the case of an external potential perturbation U and the LLN computed for a surface mass load perturbation ζ or equivalently a potential U'. They can be directly determined setting, respectively (U, U', τ, P) to (1,0,0,0) for TLN and (0,1,0,0) for LLN in system (A8) and in Table 2.

Several remarks on the numerical integration in order to perform high degree integration and avoid some numerical issues are given in the Appendix. LLN for several elastic models have already been compared in Wang *et al*. (2012) and in Na & Baek (2011). The elastic LLN and TLN computed with PREM containing a liquid core and following our integration scheme are given in Fig. 2. The values are consistent with those of Martens *et al*. (2019) calculated from *LoadDef* program, especially the asymptotic behaviour for high degrees (Farrell 1972; Martens *et al*. 2019). The low degrees are quite sensitive to the integration in the centre of the Earth which may be not exactly the same for both studies (see the Appendix) and could explain the differences observed especially for LLN (nonetheless never exceeded 0.5 per cent).

3.3 Integration for viscoelastic models

3.3.1 Viscoelastic models

In the following, we choose to construct viscoelastic models keeping the base of PREM (radial structure and variables) but considering Maxwell or Burgers models in some layers of the mantle. We do not choose continuous viscosity profiles existing in the literature (Vermeersen & Sabadini 1997; Kaufmann & Lambeck 2002; Steffen & Kaufmann 2005) because they have been computed from deformations of specific data and models. Since we aim to compare several independent geophysical processes in this study considering different viscoelastic models, the choice of non-adjusted viscosity profile (i.e. not derived from specific geophysical data) is more suitable. On the other hand, dealing with continuous radial viscosity function is equivalent to set an arbitrary large number of thin sublayers of constant viscosity which creates unnumerable normal modes. The normal mode approach using LT is thus very difficult to numerically handle because of the complex poles integration. If some mathematical tricks exist to overpass these difficulties (Tanaka *et al*. 2006; Spada & Boschi 2006), the FT provides the possibility to directly deal with these large amount of modes with a simple resampling of the discrete FT to include all the generated decay timescales. Finally, the parameters of the viscoelastic models used in this study obey the following constraints.

(i) The density ρ and the elastic moduli λ^e and μ^e are set to the PREM values.

(ii) The viscosity profile (either η^m and η^k) is divided in four main layers : Core(s) from $r = 0$ to 3480 km, lower mantle (LM) from $r =$ 3480 to 5701 km, upper mantle (UM) including transition zones from $r = 5701$ to 6346.6 km and lithosphere from $r = 6346.6$ km to the surface.

Table 3. Notations for viscoelastic rheologies used in this study where all viscosities are in Pa·s. We keep the compressible elastic moduli (λ^e, μ^e) from PREM in every layers of the earth model, we use viscoelastic model only in the mantle and we set $\mu^k = \mu^e/10$ if Burgers rheology is used in the UM.

Notation		Explanation
MAXWELL $\log(\eta^m)$	—	Maxwell homogeneous model in the whole mantle of viscosity η^m
MAXWELL $\log(\eta^m_{\rm UM}) - \log(\eta^m_{\rm LM})$	—	Maxwell model of viscosity $\eta^m_{\rm LM}$ in the lower mantle and $\eta^m_{\rm UM}$ in the upper mantle
MAXWELL $\log(\eta^m_{\rm UM}) - \log(\eta^m_{\rm LM})$ BURGER $\log(\eta^k_{\rm UM})$	—	Maxwell model of viscosity $\eta^m_{\rm LM}$ in the lower mantle and Burgers model of viscosities $\eta^m_{\rm UM}$ and $\eta^k_{\rm UM}$ in the upper mantle

(iii) The viscosities can only take constant value within each of these four layers (constant piecewise functions) and the viscosities in the Core(s) and the lithosphere are always infinite (purely elastic layers).

(iv) We set Maxwell models both in LM and UM.

(v) We can choose to set Burgers model only in UM and in that case, $\mu^k = \mu^e/10$.

The notations for the rheological models used in this paper are explained in the Table 3.

3.3.2 Frequency and degree dependence

Taking advantage of the correspondence principle stated in Section 2.4, viscoelastic Love numbers are calculated in the Fourier domain for a given viscoelastic model. As a consequence, the Lamé functions $\lambda(\omega)$ and $\mu(\omega)$ are frequency and radial dependent complex functions given in the Table 1. On the other hand, ρ_0 and g_0 remain real and depend only on r. Solving the system in the Fourier domain does not change the fundamental physical concepts neither the integration and interface conditions. We can then compute the Love numbers applying the same integration scheme than for elastic case resolving the gravito-elastic system at a given degree n and a given frequency ω_0. We note that unlike the elastic case, the inertial term proportional to $\rho\omega^2$ coming from the impulsion conservation equation is no longer neglected even if its contribution is small. The computed Love numbers are also complex values such that the imaginary part indicates the possible temporal delay (or phase delay) of the system response compared to the perturbation. This delay is entirely induced by the viscous behaviour of the system. The system can then be resonant in particular frequencies called modes depending on the viscoelastic model (Alterman *et al*. 1959; Wu & Peltier 1982).

LLN computed for four viscoelastic Maxwell models of fixed LM viscosity ($\eta^m_{\rm LM} = 10^{23}$Pa·s), are represented in Fig. 3 in function of degree and frequency. Fig. 3(a) shows the difference between the real part of viscoelastic LLN with respect to elastic ones while Fig. 3(b) represents the imaginary part of viscoelastic LLN. All the LLN presented have been computed using the integration scheme presented in Section 3 and the Appendix, and its variant for viscoelastic rheologies described above. Since we introduce viscosity only for intermediate mantle layers, the high degrees are barely affected by the changes in the earth model. For lower degrees, we see the behaviour of low-pass filter of the Maxwell function $m(\omega)$ defined in Section 2.2 : for periods shorter than the cut-off period, the viscoelastic LLN equals the elastic LLN and for periods longer than the cut-off period, the difference between the two increases. The cut-off period increases linearly with the UM viscosity in agreement with the theoretical formula $T^m = 2\pi\eta^m/\mu^e$ of Section 2.2. Taking the mean value of the PREM UM shear modulus $\bar{\mu^e} = 10^{11}$ Pa, we find $T^m = 2,\ 20,\ 2000$ and 200 000 yr for the successive represented Maxwell models. These values reported in black dotted lines are roughly consistent with the observed transition periods on the Fig. 3. For the imaginary part, the effects of viscosity seems to be bounded in a particular period interval. We also note that the main pattern in lower UM viscosity panels are unaffected as the viscosity increases except for downward shift towards higher periods. This behaviour comes from the simple rescaling of frequency ω to $\eta^m\omega/\mu^e$ such that $m(\omega)$ remains invariant as η^m increases if ω decreases. The frequency dependence of gravito-elastic equations being only in the $m(\omega)$ function (the intertial term is neglectible), the results are simply shifted of the value of the scaling factor. Such behaviour should not occur in Burgers models as the frequency dependence is much more complicated. As discussed in Section 2, the behaviour of high viscosity rheology (beyond $\eta^m = 10^{23}$ Pa.s) MAXWELL 18–23 tends to the elastic case for a large range of the spectrum such that only the larger periods (non-visible on the figure) still change. We also note that some artefacts appears in the lower viscosities at high degrees and long periods. It corresponds to a zone where the values of viscosities, periods and degrees are unrealistic for a physical use and for which the numerical integration becomes unstable.

3.3.3 Viscosity model dependence

To compare the response of different viscoelastic models at a given frequency, we represent the vertical displacement LLN h' for some Maxwell and Burgers rheologies in Fig. 4. This representation is interesting to highlight the different degree ranges delimited by the markers

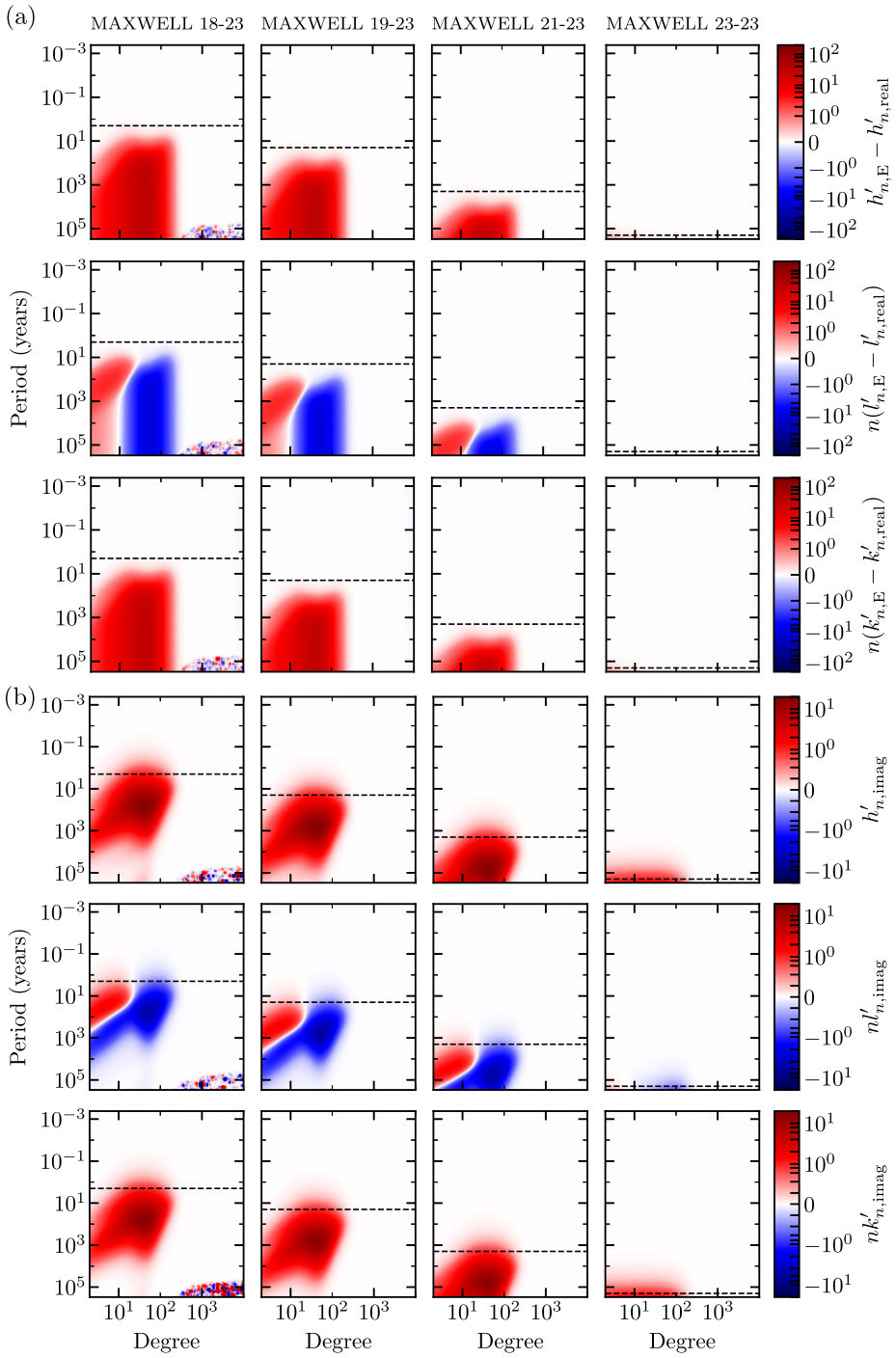

Figure 3. (a) Difference of LLN real parts in per cent between PREM and viscoelastic Maxwell models based on PREM with respective viscosity of 10^{18}, 10^{19}, 10^{21}, 10^{23} Pa·s for upper mantle and 10^{23} Pa·s for lower mantle. (b) LLN imaginary part of the models previously mentioned. The black dotted line marks the mean cut-off frequency of the equivalent low-pass filter for each model.

A to F, corresponding to the preponderance of particular viscoelastic parameters in the mantle. The period is fixed to 11 000 yr, in order to have significative effects of viscoelasticity on the LLN (Fig. 3). It is important to keep in mind that the results presented in this paragraph are applicable only at this particular frequency.

Since degree 1 (A) is mainly dependent of the Inner Core and liquid Core structure, we do not see any differences between all the models. For low degrees, we see a strong deviation of MAXWELL 21 model from the others, which is due to the differences in their LM viscosity profiles which have an impact starting from degree 2. At point B, we see the shift between models with 10^{20} Pa·s and models with 10^{21} Pa·s UM viscosity. This means that the UM structure have an influence starting from degree 3. Then from point C (degree 4), Maxwell and Burgers models with same Maxwell parameters diverge from each other. This point is the lower limit where the presence of transient

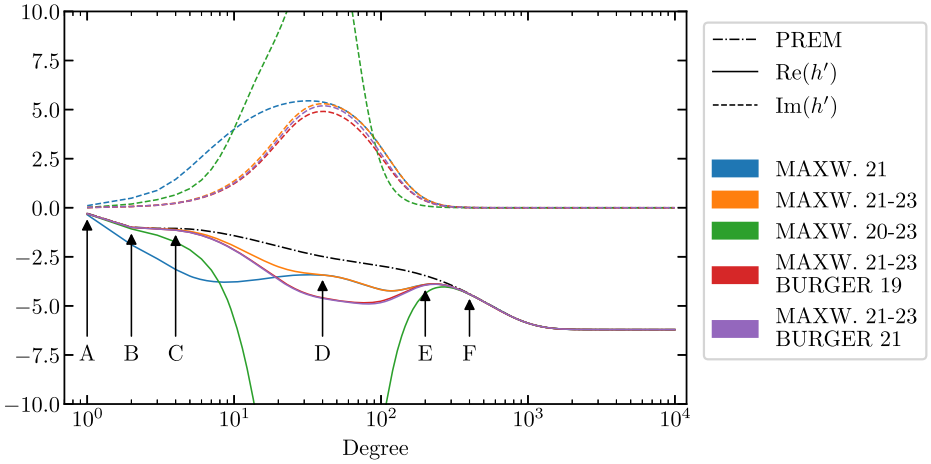

Figure 4. Real and imaginary part of vertical displacement LLN h' under an excitation of period $T = 11\,000$ yr, for several Maxwell and Burgers models of different UM and LM mantle viscosities. We also represent h' from PREM which is a real function. Points A to F indicate the main discrepancies between models.

viscosity in Burgers model infers on LLN. The value of the transient viscosity does not impact significantly the real part of LLN, but has a little influence in their imaginary part from C to E. The point D is the reconnection point for MAXWELL 21 and MAXWELL 21–23 models, defining the upper limit where LM has no more influence on LLN and from which only the UM structure infers. At point E, there are no more differences between Burgers and Maxwell models which have equal η^m while only MAXWELL 20–23 still differs from the other viscoelastic models. Finally, the point F set the limit where the mantle structure has no more influence such that LLN are impacted by the crust structure only. Consequently, modified PREM including refined crust models as CRUST1.0 should present differences beyond F.

4 COMPUTATION OF VISCOELASTIC DEFORMATION WITH FT

4.1 Sinusoidal perturbation

The complex Love numbers obtained after the integration at $\omega = \omega_0$ correspond to the frequency response of the system to a time sinusoidal unit perturbation oscillating at the frequency ω_0. Then it is easy to compute the viscoelastic deformation of a sinusoidal perturbation (such as tidal waves for example) by just multiplying the complex admittance of the perturbation derived from its sinusoid characteristics (amplitude and phase) with the associated complex viscoelastic Love number. The resulting deformation is also a sinusoid characterized by the obtained complex number.

4.2 Non-sinusoidal perturbation

We consider now the time-series of the harmonic degree n of a non-sinusoidal perturbation. To solve the problem in the frequency domain, we have to compute the discrete Fourier transform (DFT) of this signal to obtain the frequency perturbation spectrum. Then, the Earth frequency response can be computed easily by calculating the nth degree Love number for the different frequencies ω_0 of the frequency set given by the DFT. Eventually, we need to multiply the two spectra which corresponds to the convolution of the Earth response with the perturbation in the time domain. We obtain the temporal deformation after taking the inverse DFT. However, in order to avoid the calculation of Love number each time that the frequency set changes, it is easier to previously calculate the Love numbers at some well-distributed values within a large frequency range. The frequency range must include the characteristic timescales of the different geophysical phenomena that we could treat. The collection of these Love number values at these different frequencies corresponds to a good approximation of the FT of a unit impulse perturbation (temporal Dirac function). We can then linearly interpolate this Love number spectrum to the frequency set given by the DFT of any kind of perturbation.

We generally use the FFT algorithm to implement numerically the DFT. This algorithm is optimized for samples of 2^N epochs regularly spaced. Then we need to resample the initial temporal perturbation signal, especially if it is initially not regularly sampled. The resampling depends mostly on the interpolation function especially the type of spline used (linear, quadratic, cubic, ...). For high order splines (beyond cubic), the interpolated signal should create some artefacts in the frequency domain at high frequencies especially if N is too large. For linear spline, the interpolated signal could have jerky variations which create non-neglectible high frequency content which can aliased the DFT if N is not large enough (Nyquist criterion). A compromise can be made by choosing a cubic spline interpolation which should not create high frequency content because of its smoothness. Finally, we choose N in an intermediate range of values such that 2^N is large enough to avoid aliasing and not too large to avoid issues on temporal resampling. A good compromise is to choose N such that 2^{N-2} is the superiorly closest value to the number of samples in the initial series. For example if there are 500 samples in the initial time-series, the closest power of two is

$2^9 = 512$ so that we choose $N = 11$. This choice of N prevents aliasing in the spectrum calculation. If the samples are initially not regularly spaced, we should first resampling at the shortest time-step, then determine the closest power of two of the resampled time-series and finally choose the optimal N. Examples are given in Sections 5.2 and 5.3. Another trick in the computation of FFT is to artificially increase the resolution of the spectrum using zero-padding. The addition of zeros on the time-series is not without effects (windowing) on the spectrum such that we advise to not use this technique in most cases. The spectrum is less impacted by this technique if the beginning and the end of the true time-series tend to zero. Therefore, we prefer to use neither zero-padding nor windowing in this study but to compute the FFT with the same number of points (2^N) as the resampled time-series. We add a remark on the fact that since the viscoelastic Love numbers are not computed for the zero frequency, a special attention should be given to the corresponding coefficient in the DFT (leading to permanent deformation). If we only want relative values of deformations, the coefficient could simply be set to zero (the mean of the signal is then removed).

4.3 Global perturbation

The majority of perturbation signal have a non-trivial spatio-temporal repartition on the Earth surface (especially loading signals). We decompose for each time step, the spatially dependant perturbation into SH to match the decomposition of our Love number calculation. We then obtain the amplitude time-series of each SH coefficient. Then we apply to each SH coefficient time-series representing the amount of signal in a given spatial configuration the procedure described in the previous section to obtain the associated deformation SH coefficient. The recomposition of the spatio-temporal deformation is done by the recombination of all SH coefficient for each time step. We note that since the Love numbers are degenerate in the order m for a SNREI model, every (n, m) Love numbers are equal to the zonal $(n, 0)$ Love number.

This general procedure is capable of handling a large number of geophysical signals while being fairly easy to implement and numerically fast. Moreover, it is still possible in the viscoelastic case to use Green's function formalism developed in (Farrell 1972) to deal with local sinusoidal deformations. The main difference is that the Green's functions will be complex and calculated for a single frequency chosen to correspond to the perturbation signal frequency.

5 APPLICATIONS

The viscoelastic Love numbers are used in several classical applications. We consider some particular examples: long period tidal deformations, GIA and the secular signal deduced from GRACE/GRACE-FO (Gravity Recovery And Climate Experiment - Follow-On, Tapley *et al*. 2004; Flechtner *et al*. 2014), mainly due to present-day ice mass loss in Antarctica, Greenland and Alaska (Luthcke *et al*. 2013). We compare the elastic and several viscoelastic responses to these perturbation signals in order to evaluate the impact of slightly different rheologies. This can be useful to further investigate the usual models of deformation considering the actual experimental constraints. In particular, the viscoelastic long period tidal deformations are compared to the results of current IERS convention model (Petit & Luzum 2010).

5.1 Solid Earth tides

Solid Earth tides, especially their long-period zonal constituents, are particularly interesting to investigate the Earth's rheology, as the tidal potential can be computed with high precision (Hartmann & Wenzel 1995). Among other studies (Dehant & Zschau 1989; Walterova & Behounkova 2017), Benjamin *et al*. (2006) investigated the anelasticity in the Earth response to the long-period tides using C_{20} observations from Satellite Laser Ranging, and Polar Motion. However, their approach is based on the absorption band process as it is commonly done in seismology but not on a consistent viscoelastic model. We propose to calculate the direct response of several viscoelastic models based on PREM with the method developed in this study to evaluate the differences with the IERS conventions (Petit & Luzum 2010), which are classically used in the processing of geodetic data. The solid Earth tidal displacement calculation described in IERS conventions (Petit & Luzum 2010) is based on Wahr (1981) and Mathews *et al*. (1995) Love number definitions and consists of several disparate contributions to each Love numbers and displacement terms that are computed in a two steps procedure. In addition, the non-sphericity of the Earth and the Free Core Nutation resonance have been taken into account in the IERS conventions, leading to both degree and order dependence of Love numbers, and to frequency-dependant Love numbers in the diurnal band.

Since the effect of viscoelasticity in the mantle becomes significant at long periods (Fig. 3), we focus on the zonal long period tidal waves. Moreover, we will only consider the predominant zonal contribution (2,0), since the higher zonal terms are several orders of magnitude lower. We propose to represent the vertical displacements induced by these (2,0) tidal constituents for some viscoelastic models and to compare the results with the IERS conventions.

We use the catalogue corresponding to the harmonic decomposition of tidal constituents given by Doodson (1921), in the theoretical frame developed by Hartmann & Wenzel (1995). We compute the complex admittance of each wave that we then multiply with the corresponding complex degree 2 TLN to obtain the FT of the deformation as described in the Section 4.1. We compute the deformation for all the (2,0) tidal waves at their respective frequencies. The degree 2 TLN associated to the main waves are reported in Table 4 where we see that the major impact is for the longest period waves and the lowest viscous models. The total deformation spectrum is given by the collection of all Dirac

Table 4. Complex degree 2 TLN for the four main tidal waves and for each of the considered viscoelastic models.

Wave Frequency (cycle·yr^{-1})	[Nodal] 0.0537	[Ssa] 2.0000	[Mm] 13.2555	[Mf] 26.7371
MAXWELL 18	1.668203 − 0.318953i	0.647748 − 0.186672i	0.604599 − 0.030164i	0.603753 − 0.014975i
MAXWELL 19	0.929106 − 0.437636i	0.603970 − 0.020013i	0.603487 − 0.003022i	0.603479 − 0.001498i
MAXWELL 20	0.610220 − 0.073787i	0.603481 − 0.002003i	0.603476 − 0.000302i	0.603476 − 0.000150i
MAXWELL 21	0.603545 − 0.007458i	0.603476 − 0.000200i	0.603476 − 0.000030i	0.603476 − 0.000015i
MAXWELL 22	0.603477 − 0.000746i	0.603476 − 0.000020i	0.603476 − 0.000003i	0.603476 − 0.000001i
MAXWELL 23	0.603476 − 0.000075i	0.603476 − 0.000002i	0.603476 − 0.000000i	0.603476 − 0.000000i
MAXWELL 18−23	0.612103 − 0.025199i	0.603842 − 0.002128i	0.603485 − 0.000335i	0.603478 − 0.000166i
MAXWELL 19−23	0.606343 − 0.005692i	0.603480 − 0.000224i	0.603476 − 0.000034i	0.603476 − 0.000017i
MAXWELL 20−23	0.603529 − 0.000895i	0.603476 − 0.000024i	0.603476 − 0.000004i	0.603476 − 0.000002i
MAXWELL 21−23	0.603476 − 0.000156i	0.603476 − 0.000004i	0.603476 − 0.000001i	0.603476 − 0.000000i
MAXWELL 19−23 BURGER 17	0.609618 − 0.003846i	0.608544 − 0.001500i	0.604968 − 0.002329i	0.603970 − 0.001499i
MAXWELL 19−23 BURGER 19	0.608745 − 0.005928i	0.603497 − 0.000444i	0.603476 − 0.000067i	0.603476 − 0.000033i
MAXWELL 19−23 BURGER 21	0.606374 − 0.005720i	0.603480 − 0.000226i	0.603476 − 0.000034i	0.603476 − 0.000017i
MAXWELL 21−23 BURGER 17	0.608966 − 0.000157i	0.608529 − 0.001391i	0.604959 − 0.002305i	0.603967 − 0.001484i
MAXWELL 21−23 BURGER 19	0.607071 − 0.002575i	0.603486 − 0.000226i	0.603476 − 0.000034i	0.603476 − 0.000017i
MAXWELL 21−23 BURGER 21	0.603479 − 0.000239i	0.603476 − 0.000006i	0.603476 − 0.000001i	0.603476 − 0.000000i

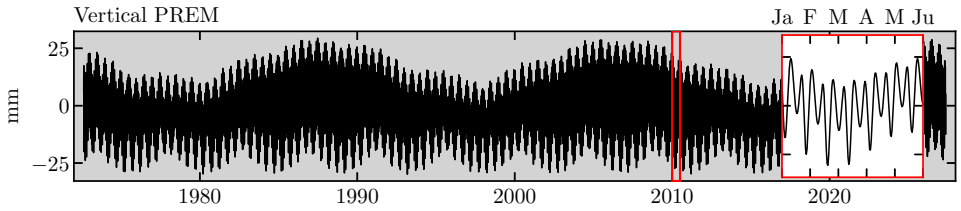

Figure 5. Elastic PREM vertical displacement of (2,0) tidal waves from Doodson catalogue. This displacement have to be multiplied by the associated Legendre polynomials to obtain the real displacement in function of latitude. The red inset is a 6 months zoom to see the high frequencies.

peaks which is none that a Fourier series as described in Beuthe (2015). At last in the time domain, the resulting time-series deformation is multiplied with the associated (2,0) Legendre polynomials to get latitude dependence.

The PREM vertical deformation without the permanent tide is shown in Fig. 5. This displacement is a reference such that the real displacement is obtain by multiplying the reference with the Legendre polynomials. The deformation waves are contained in a 18.6 yr (Nodal tide) and a 4.5 yr envelopes, which is itself modulated by the semi-annual wave (Ssa). The smaller periods especially Mm (27.55 d) and Mf (13.66 d) are visible on the red zoom inset of Fig. 5.

We then compute the tidal deformations for several viscoelastic rheologies. Fig. 6 represents the residual vertical displacement of several viscoelastic models after PREM signal was removed. The permanent tide is then automatically discarded and the signal is zero mean. The amplitude of the residuals and the corresponding normalized time-series are represented separately in order to compare properly the phase shift and the frequency content of the signal. We also include the residuals calculated from the difference between the IERS conventions (Petit & Luzum 2010) and PREM. We choose to compute the residuals for the reference displacement (without multiplying by the Legendre polynomial) because the choice of a particular latitude does not matter to compare the different models since every models are modulated by the same Legendre polynomial value at a given latitude. The reference amplitude have then to be considered as real amplitude with Legendre polynomials is equal to one (equivalent to latitude $\pm 36.5^{\circ}$N). The maximum amplitude is obtain by multiplying the reference amplitude by a factor 2.24.

The amplitude for the residuals of MAXWELL 18 and MAXWELL 19 models are ten times greater than the ones reported in the figure, reflecting the important discrepancy between these models and PREM. The amplitude decreases when the viscosity increases for homogeneous viscoelastic Maxwell models. The same behaviour is observed when we set the LM viscosity at 10^{23} Pa·s and that only the UM viscosity varies. Again the amplitude of Burgers models decreases as the transient viscosity η_k increases.

On the other hand, the right-hand panel indicates that the main component of the difference between PREM and the viscoelastic models is the Lunar nodal wave at 18.6-yr period. Indeed, as we saw in Fig. 3 for LLN, TLN are more impacted by the viscoelasticity as the period increases. The largest tidal period computed being the Nodal wave, it is the most likely one to be affected. We also see that this wave is subject to a phase shift as the viscosity changes. We can measure it by locating the maximum displacement positions on the time-series. The phase shift exists for all tidal waves but is more important for the longest periods (as they are the most likely to be impacted by the viscosity).

As every model is associated to a low pass filter with one or several cut-off frequencies, changing the viscosity model is also changing its cut-off frequencies. If the range of cut-off frequencies contains one or several of the main tidal wave, then changing even slightly the viscosity models can significantly impact the displacement of the Earth at this tidal wave frequency. We can see this effect in the Fig. 6 especially when we change the value of transient viscosity for Burgers models, but also as the global mantle viscosity increases.

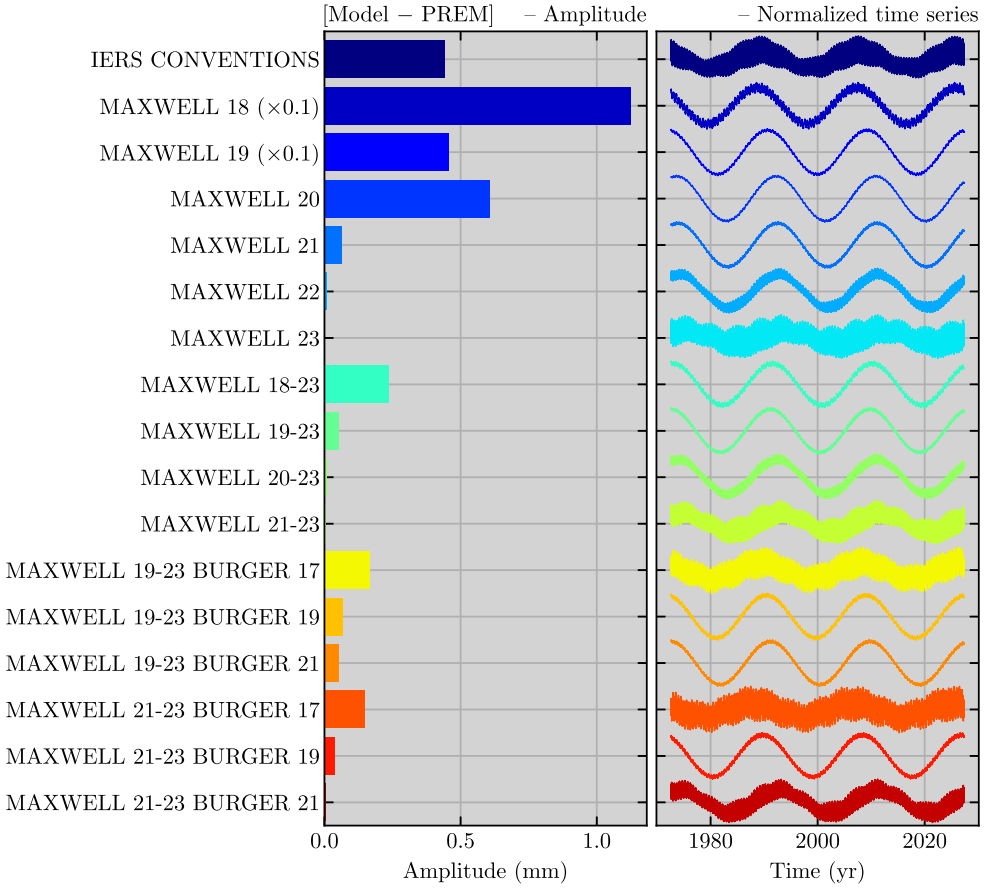

Figure 6. Residuals of the total vertical displacement generated by the (2,0) tidal waves from Doodson catalogue, for several viscoelastic rheologies and the model given in the IERS conventions (Petit & Luzum 2010). The residuals have been computed according to PREM displacement time-series. We plotted the amplitudes (left-hand panel) and the normalized time-series (right-hand panel).

We show the high dependence of the Earth viscoelastic parameters to the response of long-period tides. The objective should then to refine the determination of these parameters to provide optimal parameters for a realistic viscoelastic earth model. The use of such model in the tidal deformation computation should be able to replace the actual IERS conventions two-steps procedure which does not correspond to a consistent physical model. In particular, the differences in the 18.6-yr tide deformation between the actual IERS conventions and a more realistic viscoelastic model can exceed 2 mm (after multiplying by degree 2 Legendre polynomial), which is twice the desired accuracy in position for terrestrial reference frame (Altamimi *et al*. 2016).

5.2 GIA/postglacial rebound

GIA is another important proof of the viscoelasticity of the Earth and has already been largely studied (Peltier *et al*. 1981; Lambeck *et al*. 1998). A GIA solution (displacement rates and ice history) is generated for a given rheology and Earth structure. We want to evaluate the sensitivity of actual deformation rates observed with a slight change in viscoelastic parameters from a GIA model (Steffen & Kaufmann 2005; Roy & Peltier 2015). In the same way, Caron *et al*. (2017) used a Bayesian approach to realize such sensitivity tests on GIA models parameters. We compute the displacements given by the ICE-6G model supplied by Peltier *et al*. (2015) to validate our methodology on non-periodic perturbations. Taking the ice history derived from ICE-6G, we can compare the predicted actual vertical displacement rate for several Maxwell rheologies since they generally are the best to fit the GIA observed deformations.

First, we decompose the ice history into SH using the Python library SHTools (Wieczorek & Meschede 2018). We consider the ocean as an homogeneous reservoir and determine an homogeneous sea level at each time in order to enforce the global mass conservation. As described in Sections 4.2 and 4.3, we then compute the DFT of each SH coefficient using FFT algorithm on the time-series previously resampled to $2^{11} = 2048$ epochs by cubic interpolation. We choose $N = 11$ because the initial number of sample in the ice history is 122, extended to 489 taking the minimum time-step of 250 yr, and which the closest power of two is 2^9. Some coefficients and an example of their Fourier spectrum estimation are given in Fig. 7 where we see that choosing too small N can create aliasing and can slightly shift in the y-direction the FFT results (panel b). Since the input time-series are real, the FFT is computed only between $f = 0$ and $f = f_s/2$, where $f_s = 0.0042$ cycle·yr^{-1} is the sampling frequency. The rest of the spectrum is useless and redundant since it is symmetric. The frequency precision

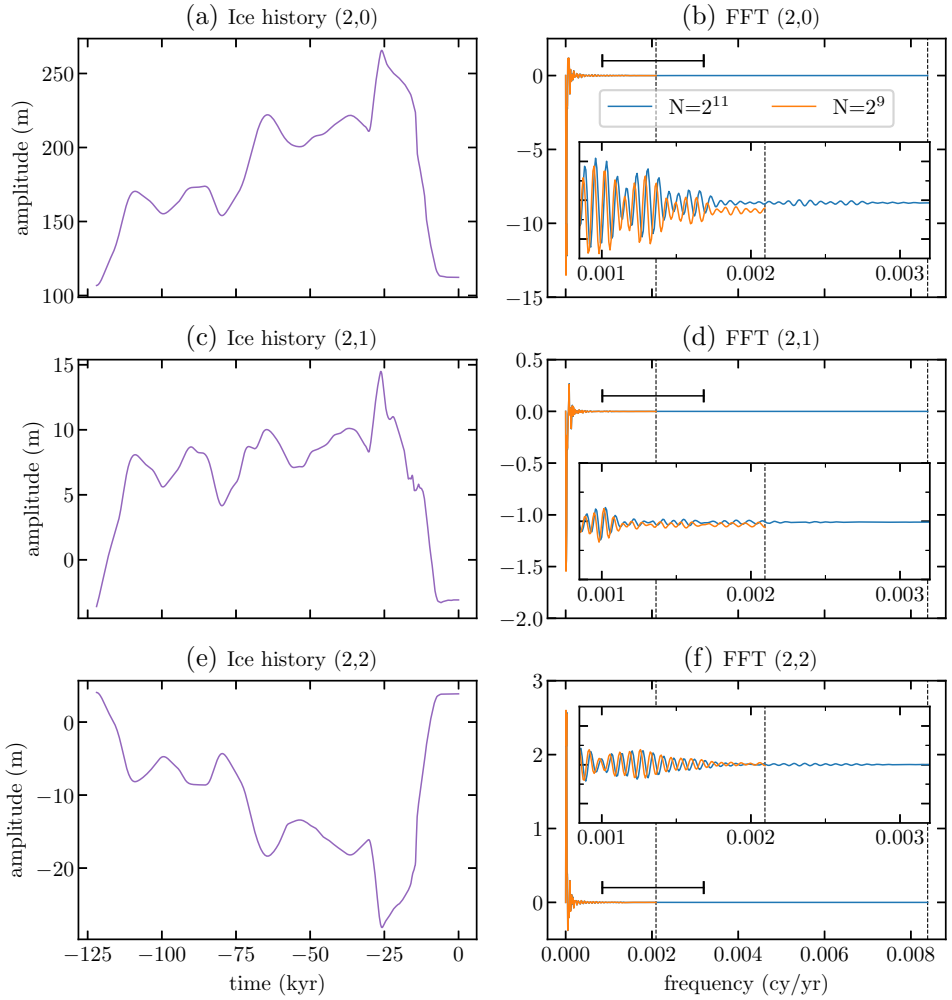

Figure 7. Cubic interpolation of time evolution and the associated FFT of (2,0), (2,1) and (2,2) SH coefficients of the ICE-6G ice history. The black dotted lines in FFT plots are the Nyquist frequencies for the two choices of N where 2^N is the number of time and frequency samples used, while the black horizontal segments are the frequency span of the inset zoom plots.

$\delta f = 1.03 \times 10^{-6}$ cycle·yr^{-1} of the FFT is given by the inverse of the total period of the ice history signal (duration of 122 kyr). It is also the most little non-zero frequency to be calculated by the FFT algorithm. After multiply coefficients and LLN spectrum and take the inverse FFT, we have the temporal deformation SH coefficients which we combine with Legendre polynomials to obtain the deformation field.

The ice history model in ICE-6G already assumes a particular rheology which was determined by the global inversion of the surface displacements and sea level data (Peltier *et al*. 2015). It is then interesting to evaluate the importance of a slight change in rheological parameters when we compute the vertical surface displacement. The results are shown in the Fig. 8, where we test five different Maxwell viscoelastic rheologies for the mantle. Their parameters have been chosen to explore the parameter space close to ICE-6G results and to be coherent with the values obtain in Kaufmann & Lambeck (2002), Steffen & Kaufmann (2005) and Caron *et al*. (2017) to recover the UM and LM viscosities. The amplitudes of the vertical rate are very similar to the one found in the viscoelastic prospection led in Marotta (2003). The amplitudes could significantly differ from ICE-6G showing the strong dependence in rheological parameters.

In order to compare the spatial repartition of the deformation between the different models and ICE-6G, we compute for each case, the normalized map (with unity maximum amplitude), and then define a correlation coefficient C as

$$C = \frac{\sum_{i,j} \left(M_{ij} - \overline{M}_{ij}\right)\left(P_{ij} - \overline{P}_{ij}\right)}{\sqrt{\sum_{i,j} \left(M_{ij} - \overline{M}_{ij}\right)^2} \sqrt{\sum_{i,j} \left(P_{ij} - \overline{P}_{ij}\right)^2}}, \tag{11}$$

such that P is the normalized ICE-6G map and M one of the normalized tested rheology map. All the models presented in the Fig. 8 have $C > 0.55$. The rheologies with the best spatial correlation to ICE-6G are MAXWELL 21–22 and MAXWELL 21–23 reaching 0.93. The optimal parameter between amplitude and spatial pattern should be $10^{21} < \eta^m_{\mathrm{UM}} < 10^{22}$ and $10^{22} < \eta^m_{\mathrm{LM}} < 10^{23}$. If these values are in a good agreement with the ICE-6G model, they have to be used with precaution and maybe locally modified or refined to integrate other timescale phenomena such as PSD or Chandler wobble. Besides, Geruo *et al*. (2013) show that the determination of optimal viscosity parameters based

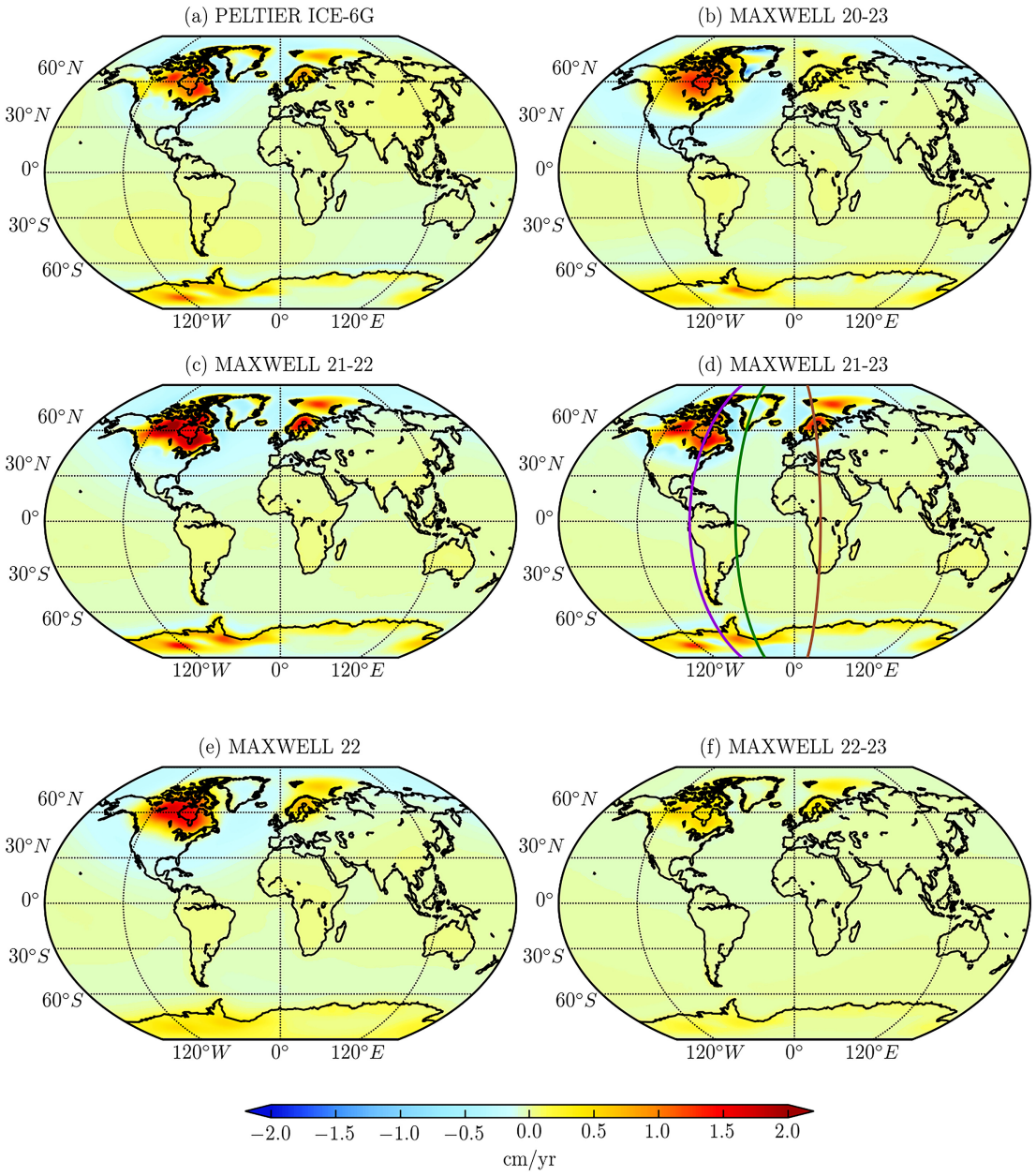

Figure 8. Actual vertical displacement rate (in cm·yr^{-1}) computed with ice history of the model ICE-6G (Peltier *et al*. 2015) for several viscoelastic rheologies. The ICE-6G actual rate map is also shown as a reference. Coloured meridians in (d) refer to slices shown in Fig. 9. The spatial correlation coefficients ($0 \leq C \leq 1$) between the normalized maps and the reference are (from (b) to (f)) : [0.57,0.93,0.93,0.79,0.87].

on local studies cannot be properly generalized in global models. Then, the 3-D structure of the earth model especially the viscosity profile, should play an important role in the observed uplift of specific regions (Wu 2006; Spada *et al*. 2006; Wu *et al*. 2013).

The optimal viscosity parameters correspond to a cut-off period of 2000 or 20 000 yr for LM and of 200 yr for UM. The deformation rate in the LM should then be much slower than in the UM where the timescale is much shorter. To investigate this, we calculated the LLN in the deep interior of the Earth from the CMB to the surface. They have been computed by saving the three unscaled propagating solutions throughout the mantle and then multiply by scaling constants determined within the LLN at the surface. The deep deformation rates have then been computed for MAXWELL 21–23 model using the same scheme than described above (with FFT) at all depth but with a zero frequency LLN taken as elastic LLN. We reported in the Fig. 9(a) these deformation rates, for the three longitude slices drawn in the Fig. 8(d). The choice of [−80°E, −45°E, +20°E] longitudes has been done to cross the areas of largest deformation: Canada, Greenland, Scandinavia and Antartica. We see that the localization of the deformation rate is mainly in the UM. This result is not surprising considering the time scales previously estimated for LM and UM. Nevertheless, this does not imply that the actual steady state deformation is null in the LM, as shown in Fig. 9(b). The actual steady-state deformation spreads in the whole mantle under the loading of actual and past ice sheets, especially in Antarctica where the actual ice thickness is the largest. Also, we see the formation of a positive deformation bulge beside the ice sheet

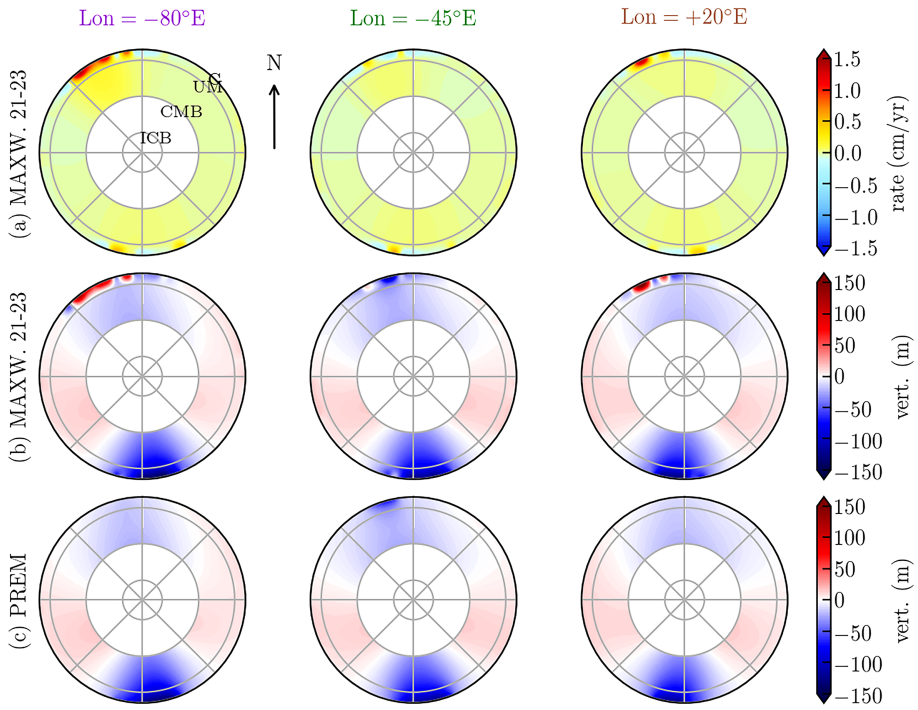

Figure 9. Vertical actual deformation rate (a) and actual steady state deformation (b, c) in the deep interior of the Earth until the CMB, along longitudinal slices pointed out by the respective coloured lines in Fig. 8(d). Panels (a, b) are related to MAXWELL 21–23 rheology and (c) to PREM.

subsidences. This is the signature of an internal redistribution of matter to reach the global deformation equilibrium state. We compare the actual steady state deformation from MAXWELL 21–23 with PREM (Fig. 9c) and see that in PREM, we only see actual ice-covered regions creating deformation since the elastic constraint in other regions (Hudson Bay, Scandinavia, ...) has already been released 1000 yr ago.

5.3 Present-day ice melting

In addition to Pleistocene deglaciation, the Earth is experiencing present-day ice melting at high latitudes (Shepherd *et al*. 2018, 2020) but also of mountainous glaciers at mid latitude (Jacob *et al*. 2012) which can be measured with various space techniques, such as altimetry (Helm *et al*. 2014) and gravimetry (Velicogna *et al*. 2020). For the smallest timescale of deformation, the impact of viscosity should be lower considering the values of η in the mantle. For example, Chanard *et al*. (2018) studied the impact of similar viscoelastic Maxwell and Burgers models to those used in this study, on the annual loading signal. They compare GNSS displacements to site displacements recovered in solving the direct problem for several rheologies applied on GRACE data. They show that the choice of rheological models does not significantly affect the annual signal in vertical time-series, but could affects the horizontal time-series. This is consistent with the previous results in this paper, as shown in Fig. 3. However, the loading signal extracted from GRACE and GRACE-FO also contains long-period signal variations, which can be due to secular climate changes (ice melting on Antarctica, Greenland and Alaska (Luthcke *et al*. 2013)) or to long period meteorological phenomena exceeding a decade (Trenberth 1990). The effects of viscoelasticity should then be more important and we choose to focus on these long periods.

Then, we use the surface mass variations deduced from GRACE and GRACE-FO during the time span 2004–2020 to access intermediate frequencies of deformation, additionally to the seasonal hydrological cycles. We use the CSR RL06 Mascons solution downloaded from http://www2.csr.utexas.edu/grace/RL06_mascons.html. This solution has been improved since the RL05 release (Save *et al*. 2016) especially in term of resolution of the supplied regular grid which allow a proper resolution of the coastlines. As a mascons technique, the RL06 solution is free of any empirical filtering and is moreover corrected from the GIA ICE6G-C from Peltier *et al*. (2015). Its low degree zonal coefficients C_{20}, C_{30} have also been replaced by those derived from Satellite Laser Ranging (Loomis *et al*. 2019). We use the same scheme than in Sections 4.3 and 5.2 to compute the displacements choosing a sampling of $2^N = 1024$ which gives a sampling frequency of $f_s = 56.38$ cycle·yr^{-1} and a frequency precision $\delta f = 0.055$ cycle·yr^{-1}.

We fit the deformation in order to only get the secular linear trend, which is the more likely to be affected by the viscoelastic rheology. This signal should denote the actual ice melting average velocity on the polar regions. We represent the associated secular displacement for different rheologies in polar regions in Fig. 10. To be consistent with the previous section, we choose to represent the displacements computed from PREM and patchy viscoelastic models. We choose first the MAXWELL 21–23 model consistent with GIA (Section 5.2) and with recent studies (Whitehouse *et al*. 2012; Peltier *et al*. 2015; Caron *et al*. 2017). Then we choose MAXWELL 18–23 to provide a model of low UM

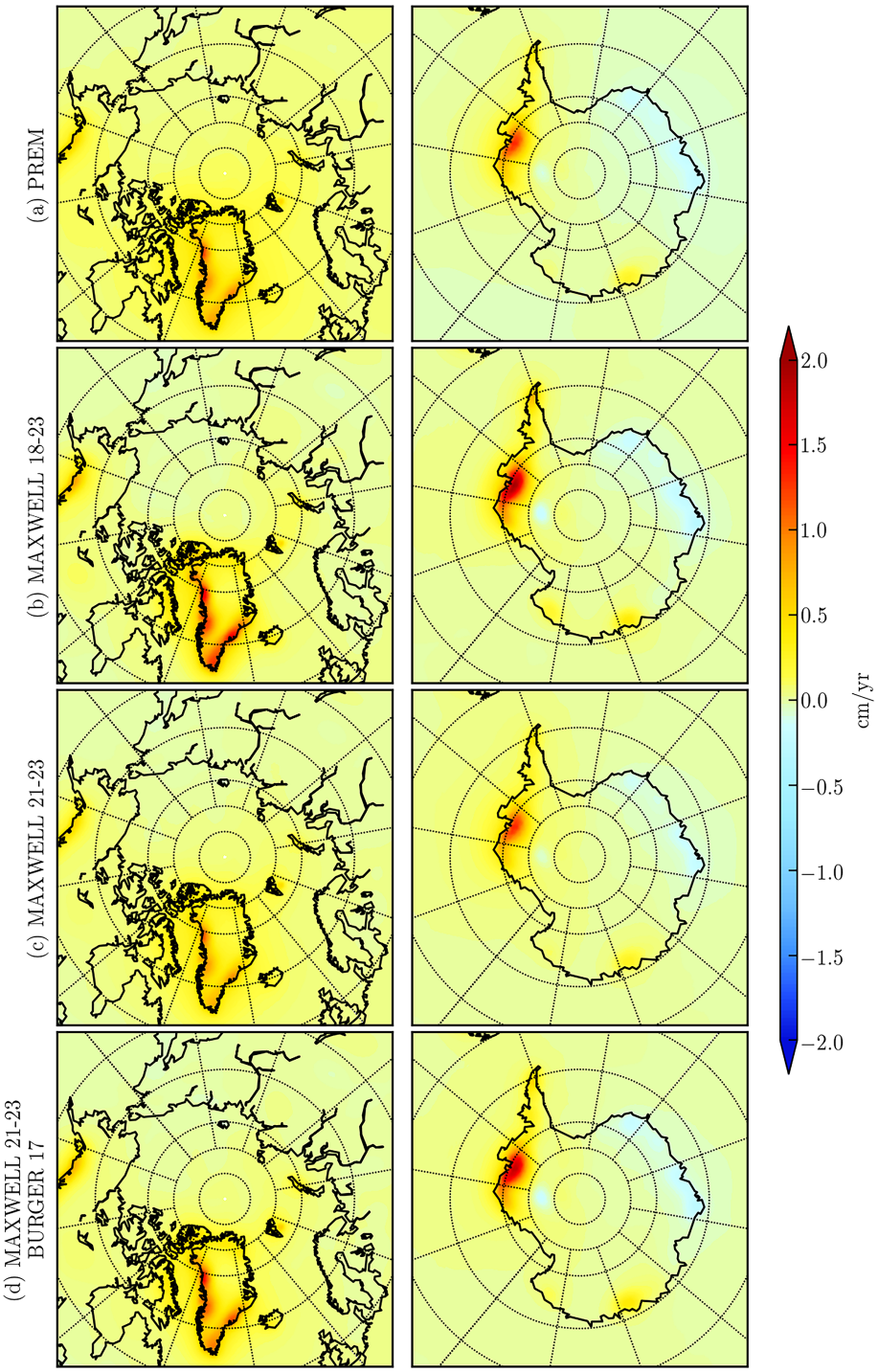

Figure 10. Actual vertical displacement rate (in cm·yr^{-1}) from the GRACE/GRACE-FO CSR data mainly due to ice melting, for several viscoelastic rheologies and PREM.

viscosity as Nield *et al*. (2014) suggested studying the Antartic Peninsula. Finally, we choose to represent a Burgers model with low transient viscosity.

The spatial pattern does not seem to radically change between the different viscoelastic rheologies and PREM except for the MAXWELL 18–23 rheology where we see higher deformation of the Antartic Peninsula (Nield *et al*. 2014) and the Greenland coast side. As we explore extremely long periods (a trend is considered as an nearly infinite period signal), the displacements computed for all rheologies are close from each other and the differences are only coming from the interannual variations of the ice mass loss. In particular, the subduction zone in south Alsaka between Pacific and North American Plate, is not very sensitive to any particular viscosity of the UM in the range proposed by the model of Jadamec *et al*. (2013): η_{UM} is from 10^{19} to 10^{21} Pa·s. In any case, it seems not reasonable to choose global value of viscosity by extrapolating from some localized subduction zones (Geruo *et al*. 2013) or local studies (Nield *et al*. 2014; Bos *et al*. 2015). The main

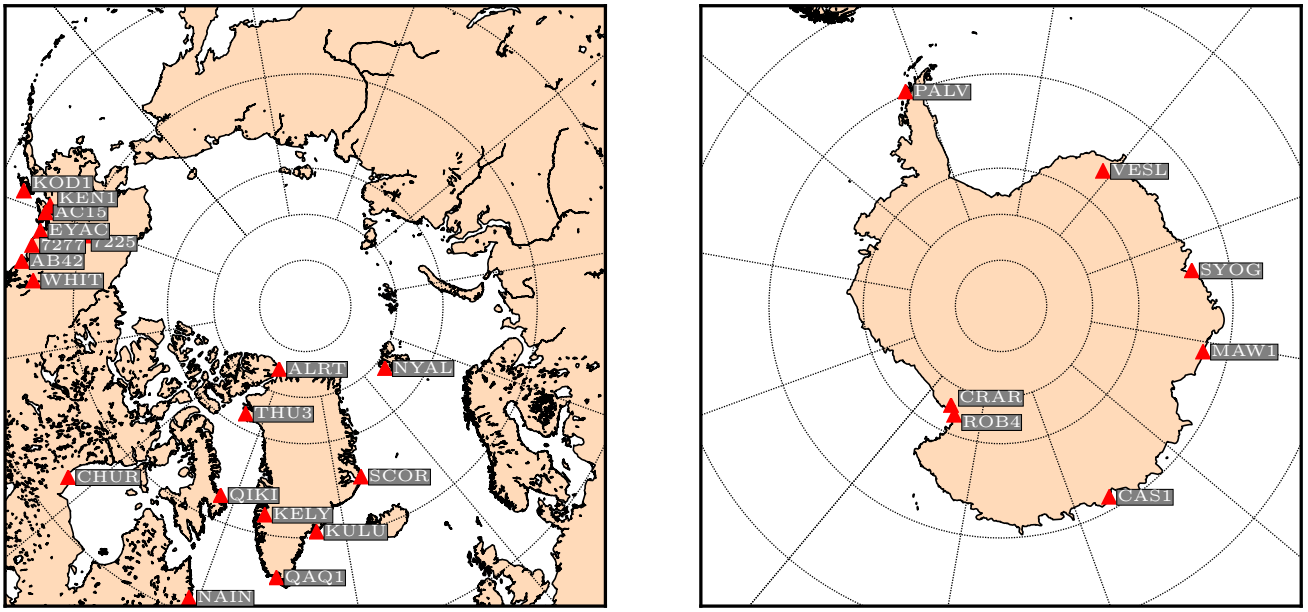

Figure 11. ITRF Stations positions for which we computed the vertical rate values in the Tables 5 and 6.

Table 5. Rates (mm·yr^{-1}) of several ITRF stations in Antarctica calculated for ITRF14 solution (Altamimi *et al*. 2016) and for different rheologies in GIA models and GRACE deformations.

ITRF site	PALV	CRAR	ROB4	CAS1	MAW1	SYOG	VESL
DOMES	66005M002	66001M004	66063M002	66011M001	66004M001	66006S002	66009M001
Lon. (°E)	295.949	166.668	163.190	110.520	062.871	039.584	357.158
Lat. (°N)	−64.775	−77.848	−77.034	−66.283	−67.605	−69.007	−71.674
ITRF Up rate	+5.865	−0.338	+1.076	+0.892	−0.546	+0.857	+0.782
Rates for GIA models							
ICE-6G	+2.469	+1.010	+0.995	+1.052	+0.414	+0.871	+1.381
MAXW21	+2.758	+2.781	+1.602	+1.996	+0.631	+1.201	+1.314
MAXW21–22	+3.330	+4.525	+3.229	+2.895	+1.493	+2.099	+2.293
MAXW21–23	+3.081	+3.765	+2.592	+2.783	+1.348	+2.005	+2.096
MAXW21–23 BURGER 17	+2.938	+3.608	+2.506	+2.694	+1.331	+1.952	+2.034
Rates for GRACE data (without ICE-6G)							
PREM	+1.230	−0.027	−0.063	+0.750	−0.868	−1.311	−1.568
MAXW21	+1.499	+0.335	+0.300	+1.059	−0.532	−0.967	−1.222
MAXW21–22	+1.498	+0.334	+0.300	+1.059	−0.532	−0.967	−1.222
MAXW21–23	+1.498	+0.334	+0.300	+1.059	−0.532	−0.967	−1.222
MAXW21–23 BURGER 17	+2.058	+0.267	+0.231	+1.478	−0.634	−1.254	−1.675

difference between models is the maximum value of the slope going from 1.3 cm·yr^{-1} for elastic and MAXWELL 21–23 until 1.8 cm·yr^{-1} adding a BURGER 17 and reaching 2.0 cm·yr^{-1} for the MAXWELL 18–23. It was predictable regarding Fig. 3, that the low viscosity models impact the most the deformation rate observed. The maximum vertical rates derived from ICESat in the Greenland are close to the one of PREM and MAXWELL 21–23, according to previous studies (Spada *et al*. 2012; Groh *et al*. 2014; Wang *et al*. 2018). These maximum rates are very localized in the west and southeast coasts but close to zero in the north east. Concerning Antarctica, we find the well-known ice melting uplift on the Pine Island Bay, the Byers Peninsula and the Budd coast while the west Antarctica subsides upon a thicker ice cap.

The great similarity between all of the presented models, for these range of frequencies, are maybe due to the fact that the model does not take into account the longitudinal and latitudinal dependence of the viscoelastic parameters, which can change the local uplift models such as the subduction zone of South Alaska (Jadamec *et al*. 2013). Also, taking into account time dependent velocities in polar ice melting should have an effect in the recovery of shorter period displacements even if the importance of viscoelasticity decreases with the period (Fig. 3). Despite, the global isotropic layered model provides interesting results, since we can compute deformations for very low degrees, along with local deformations that are consistent with (but not as precise as) local laterally heterogeneous models.

We finally compared the uplift rate of several ITRF2014 geodetic stations (Altamimi *et al*. 2016) shown in Fig. 11 at high latitude (Arctic and Antarctica) with the rates of some viscoelastic models (GIA and present-day ice melting) evaluated in this study (Tables 5 and 6). The

Table 6. Rates (mm·yr^{-1}) of several ITRF stations around the North Pole calculated for ITRF14 solution (Altamimi *et al*. 2016) and for different rheologies in GIA models and GRACE deformations.

ITRF site	CHUR	NAIN	QIKI	ALRT	THU3	KELY	QAQ1	KULU	SCOR
DOMES	40128M002	40164M001	40166M001	40162M001	43001M002	43005M002	43007M001	43003M001	43006M002
Lon. (°E)	265.911	298.311	295.966	297.660	291.175	309.055	313.952	322.851	338.050
Lat. (°N)	+58.759	+56.537	+67.559	+82.494	+76.537	+66.987	+60.715	+65.579	+70.485
ITRF Up rate	+10.96	+4.491	+4.073	+6.194	+6.240	+2.415	+4.684	+7.110	+4.055
Rates for GIA models									
ICE-6G	+8.588	+2.012	−1.448	+3.877	−0.116	+0.674	+2.497	−0.516	+1.592
MAXW21	+0.952	+1.441	−4.574	+5.211	−3.489	+1.168	+1.993	−0.546	+1.944
MAXW21–22	+14.775	+5.127	−1.080	+4.513	−2.261	+2.473	+1.572	−0.752	+0.918
MAXW21–23	+8.508	+2.989	−2.761	+4.759	−2.916	+2.508	+2.071	+0.153	+1.630
MAXW21–23 BURGER 17	+8.557	+2.967	−2.655	+4.578	−2.884	+2.483	+1.873	+0.113	+1.512
Rates for GRACE data (without ICE-6G)									
PREM	+0.692	+0.941	+3.029	+2.945	+7.105	+7.929	+6.492	+6.881	+2.263
MAXW21	+0.374	+0.572	+2.521	+2.454	+6.556	+7.340	+5.983	+6.314	+1.769
MAXW21–22	+0.374	+0.572	+2.521	+2.453	+6.556	+7.340	+5.982	+6.313	+1.768
MAXW21–23	+0.374	+0.572	+2.521	+2.453	+6.556	+7.340	+5.982	+6.313	+1.768
MAXW21–23 BURGER 17	+0.320	+0.424	+2.557	+2.742	+8.032	+9.331	+7.813	+7.963	+1.647

ITRF site	NYAL	KOD1	KEN1	AC15	EYAC	7277	7225	AB42	WHIT
DOMES	10317M001	40419S001	49995S001	49397M001	49402M001	40416M001	40408S002	49377M001	40136M001
Lon. (°E)	011.865	207.807	208.650	210.276	214.250	217.514	212.502	221.101	224.778
Lat. (°N)	+78.930	+57.618	+60.675	+60.481	+60.549	+60.081	+64.978	+59.340	+60.751
ITRF Up rate	+6.813	+7.608	+11.24	+7.026	+1.325	+24.59	+1.595	+17.52	+1.551
Rates for GIA models									
ICE-6G	+0.635	−0.289	+0.311	+0.361	+0.524	+0.485	−0.661	+0.461	+1.572
MAXW21	−0.130	+0.504	+1.425	+1.077	+0.315	−0.224	−0.442	−0.119	+1.180
MAXW21–22	+0.729	−1.212	−0.170	−0.443	−0.790	−0.716	−1.826	+0.392	+3.567
MAXW21–23	+0.676	−0.547	+0.336	−0.043	−0.731	−0.974	−1.716	−0.243	+2.336
MAXW21–23 BURGER 17	+0.650	−0.562	+0.292	−0.075	−0.741	−0.971	−1.703	−0.254	+2.282
Rates for GRACE data (without ICE-6G)									
PREM	+2.470	+0.835	+2.265	+2.998	+4.472	+5.745	+0.989	+5.698	+1.848
MAXW21	+2.017	+0.537	+1.936	+2.662	+4.118	+5.382	+0.652	+5.336	+1.492
MAXW21–22	+2.017	+0.537	+1.937	+2.663	+4.118	+5.383	+0.652	+5.337	+1.493
MAXW21–23	+2.017	+0.537	+1.937	+2.663	+4.118	+5.383	+0.652	+5.337	+1.493
MAXW21–23 BURGER 17	+2.366	+0.518	+2.529	+3.512	+5.584	+7.290	+0.590	+7.129	+1.861

differences between the observed and modelled rates are quite sensitive to the localization of the stations and moreover to the rheological parameters for the GIA part. As discussed before, we see that the GRACE long-term signal is less affected by changing rheological parameters. To recover a consistent rate derived from GIA and present-day ice melting, present-day ice melting rates have to be combined with the ICE-6G rates, to be consistent with the models removed from the GRACE data used in this study. The difference of rates between ITRF and models can be explained by the interpolation of station position on the rough $1^\circ \times 1^\circ$ grids of the models, especially for stations on the seashore. The differences between elastic and viscoelastic modelled deformations due to present-day ice melting always exceed 0.1 mm·yr^{-1}, which is the desired accuracy of the terrestrial reference frame (Altamimi *et al*. 2016). In Greenland, these differences reach more than 0.5 mm·yr^{-1}. We note a systematic deviation from the elastic case for Maxwell models of mean −0.4 mm·yr^{-1} in north pole and +0.3 mm·yr^{-1} in south pole. This signal could be, among others, the signature of odd low degrees zonal deformations (including degree 1 along the *Z*-axis) and highlights the great dependence of the low degrees to viscosity of the mantle (Fig. 4).

6 DISCUSSION

We note an inconsistency in the choice of an Earth rheological model between solid Earth tides in the IERS Convention (Petit & Luzum 2010), deformation due to GIA and present-day ice melting. We compute the viscoelastic deformation for these three geophysical effects using consistent earth models, based on PREM model (Dziewonski & Anderson 1981), in which we added anelastic parameters in the mantle layers.

For the vertical displacement, we show that the differences between the IERS Convention (Petit & Luzum 2010) and more realistic viscoelastic models could exceed 1 mm for the 18.6-yr Lunar node tide. Such models should be tested in the processing of geodetic techniques (GNSS, DORIS, VLBI and SLR) long record (more than 20 yr), in order to improve the realization of terrestrial reference frame.

We also show that the mantle anelasticity is no longer negligible in the vertical displacements due to present-day ice melting in polar regions (see also Métivier *et al*. 2020). Indeed, the characteristic timescales (20–30 yr) are comparable to the Lunar node tide. If the spatial patterns are not very different between the elastic and viscoelastic models, the differences always exceed 0.1 mm·yr^{-1} in polar areas, and sometimes more than 0.5 mm·yr^{-1} in Greenland. Similarly to the tidal deformations, we observe that the introduction of mantle viscosity affects mostly the low degrees. In particular, the Fig. 3 shows that degree 1 is significatively affected by the viscosity profile. As it is important to accurately study the geocentre motion (Blewitt 2003; Métivier *et al*. 2010; Wu *et al*. 2012), which is particularly affected by present-day ice melting (Métivier *et al*. 2020), a viscoelastic approach should then be adopted in future models and characterization.

However, including mantle anelasticity for the present-day ice melting raises some issues about the consistency of the estimation of displacements along with the GIA. In order to properly isolate the two contributions, the same viscoelastic model should be used for both determination of long term ice history and recent ice melting, which can be measured with altimetry (Helm *et al*. 2014) and gravity (Luthcke *et al*. 2013; Velicogna *et al*. 2020) missions. This requires a great effort of computation since any GIA model should then be produced in a self-consistent manner with a present-day ice melting model. Moreover, the great variability of deformation measured with geodetic techniques between nearby stations (Tables 6 and 5) suggests inhomogeneous values of viscoelastic parameters in the mantle at various spatial scales (Métivier & Conrad 2008; Nield *et al*. 2014; Bos *et al*. 2015). This could largely influence past and present ice models and make their determination more complex. Unfortunately, the theoretical frame used to calculate Love numbers is for now not suited to take into account the spatial heterogeneities of the Earth structure, and should then be reviewed. This have already been done partially when we consider the ellipticity of the Earth (Métivier *et al*. 2005) for example.

ACKNOWLEDGEMENTS

This work was partially supported by the CNES (Centre National d'Etudes Spatiales). We thank the editor D. Agnew and the two anonymous reviewers for their constructive comments and remarks improving the clarity of this manuscript and the discussion about the Fourier method. AM and JPB designed the study. AM computed the Love numbers, developed the Fourier method and computed the deformations. AM wrote the preliminary draft. AM and JPB analysed the results and contributed to the original version before approved the published version of the manuscript.

DATA AVAILABILITY

The data underlying this paper are available in the paper and in its online supplementary material.

REFERENCES

Geruo, A., Wahr, J. & Zhong, S., 2013. Computations of the viscoelastic response of a 3-D compressible Earth to surface loading: an application to glacial isostatic adjustment in Antarctica and Canada, *Geophys. J. Int.,* **192**(2), 557–572.

Altamimi, Z., Rebischung, P., Métivier, L. & Collilieux, X., 2016. ITRF2014: a new release of the International Terrestrial Reference Frame modeling nonlinear station motions, *J. geophys. Res.,* **121**(8), 6109–6131.

Alterman, Z., Jarosch, H. & Pekeris, C.L., 1959. Oscillations of the Earth, *Proc. R. Soc. Lond., A,* **252**(1268), 80–95.

Agnew, D.C., 2015. Earth tides, *Treatise on Geophysics,* 2nd edn, Vol. **3,** pp. 151–178, Elsevier.

Argus, D.F., Fu, Y. & Landerer, F.W., 2014. Seasonal variation in total water storage in California inferred from GPS observations of vertical land motion, *Geophys. Res. Lett.,* **41**(6), 1971–1980.

Argus, D.F., Peltier, W.R., Drummond, R. & Moore, A.W., 2014. The Antarctica component of postglacial rebound model ICE-6G_C (VM5a) based on GPS positioning, exposure age dating of ice thicknesses, and relative sea level histories, *Geophys. J. Int.,* **198**(1), 537–563.

Argus, D.F. *et al.*, 2017. Sustained water loss in California's mountain ranges during severe drought from 2012 to 2015 inferred from GPS, *J. geophys. Res.,* **122**(12), 10–559.

Benjamin, D., Wahr, J., Ray, R.D., Egbert, G.D. & Desai, S.D., 2006. Constraints on mantle anelasticity from geodetic observations, and implications for the J2 anomaly, *Geophys. J. Int.,* **165**(1), 3–16.

Beuthe, M., 2015. Tides on Europa: The membrane paradigm, *Icarus,* **248,** 109–134.

Blewitt, G., 2003. Self-consistency in reference frames, geocenter definition, and surface loading of the solid Earth, *J. geophys. Res.,* **108**(B2), doi:10.1029/2002JB002082.

Blewitt, G., Hammond, W.C. & Kreemer, C., 2018. Harnessing the GPS data explosion for interdisciplinary science, *Eos,* **99,** 1–2.

Blewitt, G., Kreemer, C., Hammond, W.C. & Gazeaux, J., 2016. MIDAS robust trend estimator for accurate GPS station velocities without step detection, *J. geophys. Res.,* **121**(3), 2054–2068.

Bos, M.S., Penna, N.T., Baker, T.F. & Clarke, P.J., 2015. Ocean tide loading displacements in western Europe: 2. GPS-observed anelastic dispersion in the asthenosphere, *J. geophys. Res.,* **120**(9), 6540–6557.

Caron, L., Métivier, L., Greff-Lefftz, M., Fleitout, L. & Rouby, H., 2017. Inverting glacial isostatic adjustment signal using Bayesian framework and two linearly relaxing rheologies, *Geophys. J. Int.,* **209**(2), 1126–1147.

Carrere, L., Lyard, F., Cancet, M., Guillot, A. & Picot, N., 2016. FES2014, a new tidal model: validation results and perspectives for improvements, in *Proceedings of the ESA Living Planet Symposium,* pp. 9–13.

Chanard, K., Fleitout, L., Calais, E., Barbot, S. & Avouac, J.P., 2018. Constraints on transient viscoelastic rheology of the asthenosphere from seasonal deformation, *Geophys. Res. Lett.,* **45**(5), 2328–2338.

Chinnery, M.A., 1975. The static deformation of an earth with a fluid core: a physical approach, *Geophys. J. Int.,* **42**(2), 461–475.

Dehant, V. & Zschau, J., 1989. The effect of mantle inelasticity on tidal gravity: a comparison between the spherical and the elliptical Earth model, *Geophys. J. Int.,* **97**(3), 549–555.

Doodson, A.T., 1921. The harmonic development of the tide-generating potential, *Proc. R. Soc. Lond., A,* **100**(704), 305–329.

Dziewonski, A.M. & Anderson, D.L., 1981. Preliminary reference Earth model, *Phys. Earth planet. Inter.,* **25**(4), 297–356.
Farrell, W.E., 1972. Deformation of the Earth by surface loads, *Rev. Geophys.,* **10**(3), 761–797.
Flechtner, F., Morton, P., Watkins, M. & Webb, F., 2014. *Status of the GRACE Follow-On Mission, Gravity, Geoid and Height Systems,* pp. 117–121, Springer, doi:10.1007/978-3-319-10837-7_15.
Greff-Lefftz, M., Métivier, L. & Legros, H., 2005. Analytical solutions of love numbers for a hydrostatic ellipsoidal incompressible homogeneous Earth, *Celest. Mech. Dyn. Astron.,* **93**(1–4), 113–146.
Groh, A., Ewert, H., Fritsche, M., Rülke, A., Rosenau, R., Scheinert, M. & Dietrich, R., 2014. Assessing the current evolution of the Greenland Ice Sheet by means of satellite and ground-based observations, *Surv. Geophys.,* **35**(6), 1459–1480.
Hartmann, T. & Wenzel, H.G., 1995. The HW95 tidal potential catalogue, *Geophys. Res. Lett.,* **22**(24), 3553–3556.
Helm, V., Humbert, A. & Miller, H., 2014. Elevation and elevation change of Greenland and Antarctica derived from CryoSat-2, *Cryosphere,* **8,** 1539–1559.
Hinderer, J. & Legros, H., 1989. Elasto-gravitational deformation, relative gravity changes and Earth dynamics, *Geophys. J. Int.,* **97**(3), 481–495.
Jacob, T., Wahr, J., Pfeffer, W.T. & Swenson, S., 2012. Recent contributions of glaciers and ice caps to sea level rise, *Nature,* **482,** 514–518.
Jadamec, M.A., Billen, M.I. & Roeske, S.M., 2013. Three-dimensional numerical models of flat slab subduction and the Denali fault driving deformation in south-central Alaska, *Earth planet. Sci. Lett.,* **376,** 29–42.
Kachuck, S.B., Cathles & L.M. III, 2019. Benchmarked computation of time-domain viscoelastic Love numbers for adiabatic mantles, *Geophys. J. Int.,* **218**(3), 2136–2149.
Kaufmann, G. & Lambeck, K., 2002. Glacial isostatic adjustment and the radial viscosity profile from inverse modeling, *J. geophys. Res.,* **107**(B11), ETG 5–1-ETG 5-15.
Kustowski, B., Ekström, G. & Dziewoński, A.M., 2008. Anisotropic shear-wave velocity structure of the Earth's mantle: a global model, *J. geophys. Res.,* **113,** doi:10.1029/2007JB005169.
Lambeck, K., Smither, C. & Johnston, P., 1998. Sea-level change, glacial rebound and mantle viscosity for northern Europe, *Geophys. J. Int.,* **134**(1), 102–144.
Laske, G., Masters, G., Ma, Z. & Pasyanos, M., 2013. Update on CRUST1.0—a 1-degree Global Model of Earth's Crust, *Geophys. Res. Abstracts,* **15,** Abstract EGU2013-2658.
Lee, E.H., 1955. Stress analysis in visco-elastic bodies, *Quart. Appl. Math.,* **13**(2), 183–190.
Lee, E.H., Radok, J.R. M. & Woodward, W.B., 1959. Stress analysis for linear viscoelastic materials, *Trans. Soc. Rheol.,* **3**(1), 41–59.
Li, W., Shum, C.K., Li, F., Zhang, S., Ming, F., Chen, W. & Zhang, Q., 2020. Contributions of Greenland GPS observed deformation from multisource mass loading induced seasonal and transient signals, *Geophys. Res. Lett.,* **47**(15) , doi:10.1029/2020GL088627.
Longman, I.M., 1962. A Green's function for determining the deformation of the Earth under surface mass loads: 1. Theory, *J. geophys. Res.,* **67**(2), 845–850.
Longman, I.M., 1963. A Green's function for determining the deformation of the Earth under surface mass loads: 2. Computations and numerical results, *J. geophys. Res.,* **68**(2), 485–496.
Loomis, B.D., Rachlin, K.E. & Luthcke, S.B., 2019. Improved Earth oblateness rate reveals increased ice sheet losses and mass-driven sea level rise, *Geophys. Res. Lett.,* **46,** 6910–6917.
Love, A.E. H., 1911. *Some Problems of Geodynamics,* Cambridge Univ. Press.
Luthcke, S.B., Sabaka, T.J., Loomis, B.D., Arendt, A.A., McCarthy, J.J. & Camp, J., 2013. Antarctica, Greenland and Gulf of Alaska land-ice evolution from an iterated GRACE global mascon solution, *J. Glaciol.,* **59**(216), 613–631.
Marotta, A.M., 2003. Benefits from GOCE within solid Earth geophysics, *Space Sci. Rev.,* **108,** 95–104.
Martens, H.R., Simons, M., Owen, S. & Rivera, L., 2016. Observations of ocean tidal load response in South America from subdaily GPS positions, *Geophys. J. Int.,* **205**(3), 1637–1664.
Martens, H.R., Rivera, L., Simons, M. & Ito, T., 2016. The sensitivity of surface mass loading displacement response to perturbations in the elastic structure of the crust and mantle, *J. geophys. Res.,* **121**(5), 3911–3938.
Martens, H.R., Rivera, L. & Simons, M., 2019. LoadDef: a Python-based toolkit to model elastic deformation caused by surface mass loading on spherically symmetric bodies, *Earth Space Sci.,* **6**(2), 311–323.
Mathews, P.M., Buffett, B.A. & Shapiro, I.I., 1995. Love numbers for a rotating spheroidal Earth: new definitions and numerical values, *Geophys. Res. Lett.,* **22**(5), 579–582.
Métivier, L., Greff-Lefftz, M. & Diament, M., 2005. A new approach to computing accurate gravity time variations for a realistic earth model with lateral heterogeneities, *Geophys. J. Int.,* **162**(2), 570–574.
Métivier, L. & Conrad, C.P., 2008. Body tides of a convecting, laterally heterogeneous, and aspherical Earth, *J. geophys. Res.,* **113**(B11), doi:10.1029/2007JB005448.
Métivier, L., Greff-Lefftz, M. & Altamimi, Z., 2010. On secular geocenter motion: the impact of climate changes, *Earth planet. Sci. Lett.,* **296**(3–4), 360–366.
Métivier, L., Rouby, H., Rebischung, P. & Altamimi, Z., 2020. ITRF2014, earth figure changes, and geocenter velocity: Implications for GIA and recent ice melting, *J. geophys. Res.,* **125,** e2019JB018333, doi:0.1029/2019JB018333.
Na, S.H. & Baek, J., 2011. Computation of the load Love number and the load Green's function for an elastic and spherically symmetric earth, *J. Korean Physic. Soc.,* **58**(5), 1195–1205.
Nield, G.A. *et al.*, 2014. Rapid bedrock uplift in the Antarctic Peninsula explained by viscoelastic response to recent ice unloading, *Earth planet. Sci. Lett.,* **397,** 32–41.
Peltier, W.R., 1974. The impulse response of a Maxwell Earth, *Rev. Geophys.,* **12**(4), 649–669.
Peltier, W.R., Wu, P. & Yuen, D.A., 1981. The viscosities of the Earth's mantle, *Anelast. Earth,* **4,** 59–77.
Peltier, W.R., Argus, D.F. & Drummond, R., 2015. Space geodesy constrains ice age terminal deglaciation: The global ICE-6G_C (VM5a) model, *J. geophys. Res.,* **120**(1), 450–487.
Petit, G. & Luzum, B., 2010. IERS conventions (2010) (No. IERS-TN-36), Bureau International Des Poids Et Mesures, Sèvres (FRANCE).
Ranalli, G., 1995. *Rheology of the Earth,* Springer Science & Business Media.
Roy, K. & Peltier, W.R., 2015. Glacial isostatic adjustment, relative sea level history and mantle viscosity: reconciling relative sea level model predictions for the US East coast with geological constraints, *Geophys. J. Int.,* **201**(2), 1156–1181.
Sabadini, R., Yuen, D.A. & Boschi, E., 1982. Polar wandering and the forced responses of a rotating, multilayered, viscoelastic planet, *J. geophys. Res.,* **87**(B4), 2885–2903.
Sabadini, R., Vermeersen, B. & Cambiotti, G., 2016. *Global Dynamics of the Earth,* Springer Netherlands.
Save, H., Bettadpur, S. & Tapley, B.D., 2016. High-resolution CSR GRACE RL05 mascons, *J. geophys. Res.,* **121**(10), 7547–7569.
Shepherd, A., Ivins, E., Rignot *et al.*, 2018. Mass balance of the Antarctic Ice Sheet from 1992 to 2017, *Nature,* **558,** 219–222.
Shepherd, A., Ivins, E., Rignot, E. *et al.*, 2020. Mass balance of the Greenland Ice Sheet from 1992 to 2018, *Nature,* **579**(7798), 233–239.
Spada, G., Antonioli, A., Cianetti, S. & Giunchi, C., 2006. Glacial isostatic adjustment and relative sea-level changes: the role of lithospheric and upper mantle heterogeneities in a 3-D spherical Earth, *Geophys. J. Int.,* **165**(2), 692–702.
Spada, G. & Boschi, L., 2006. Using the Post-Widder formula to compute the Earth's viscoelastic Love numbers, *Geophys. J. Int.,* **166**(1), 309–321.
Spada, G., 2008. ALMA, a Fortran program for computing the viscoelastic Love numbers of a spherically symmetric planet, *Comput. Geosci.,* **34**(6), 667–687.

Spada, G. *et al.*, 2011. A benchmark study for glacial isostatic adjustment codes, *Geophys. J. Int.,* **185**(1), 106–132.
Spada, G., Ruggieri, G., Sorensen, L.S., Nielsen, K., Melini, D. & Colleoni, F., 2012. Greenland uplift and regional sea level changes from ICESat observations and GIA modelling, *Geophys. J. Int.,* **189**(3), 1457–1474.
Spada, G., 2013. Love numbers of a generalized Maxwell sphere, *Stud. Geophys. Geod.,* **57**(1), 1–16.
Steffen, H. & Kaufmann, G., 2005. Glacial isostatic adjustment of Scandinavia and northwestern Europe and the radial viscosity structure of the Earth's mantle, *Geophys. J. Int.,* **163**(2), 801–812.
Tanaka, Y., Okuno, J. & Okubo, S., 2006. A new method for the computation of global viscoelastic post-seismic deformation in a realistic earth model (I)—vertical displacement and gravity variation, *Geophys. J. Int.,* **164**(2), 273–289.
Tapley, B.D., Bettadpur, S., Ries, J.C., Thompson, P.F. & Watkins, M.M., 2004. GRACE measurements of mass variability in the Earth system, *Science,* **305**(5683), 503–505.
Tobie, G., Mocquet, A. & Sotin, C., 2005. Tidal dissipation within large icy satellites: applications to Europa and Titan, *Icarus,* **177**(2), 534–549.
Trenberth, K.E., 1990. Recent observed interdecadal climate changes in the Northern Hemisphere, *Bull. Am. Meteorol. Soc.,* **71**(7), 988–993.
Velicogna, I. *et al.*, 2020. Continuity of ice sheet mass loss in Greenland and Antarctica from the GRACE and GRACE follow-on missions, *Geophys. Res. Lett.,* **47,** e2020GL087291 , doi:0.1029/2020GL087291.
Vermeersen, L.A., Sabadini, R. & Spada, G., 1996. Analytical visco-elastic relaxation models, *Geophys. Res. Lett.,* **23**(7), 697–700.
Vermeersen, L.L. A. & Sabadini, R., 1997. A new class of stratified viscoelastic models by analytical techniques, *Geophys. J. Int.,* **129**(3), 531–570.
Wahr, J.M., 1981. Body tides on an elliptical, rotating, elastic and oceanless Earth, *Geophys. J. Int.,* **64**(3), 677–703.
Walterova, M. & Behounkova, M., 2017. Tidal effects in differentiated viscoelastic bodies: a numerical approach, *Celest. Mech. Dyn. Astron.,* **129**(1–2), 235–256.
Wang, H., Xiang, L., Jia, L., Jiang, L., Wang, Z., Hu, B. & Gao, P., 2012. Load Love numbers and Green's functions for elastic Earth models PREM, iasp91, ak135, and modified models with refined crustal structure from Crust 2.0, *Comput. Geosci.,* **49,** 190–199.
Wang, S.Y., Chen, J.L., Wilson, C.R., Li, J. & Hu, X., 2018. Reconciling GRACE and GPS estimates of long-term load deformation in southern Greenland, *Geophys. J. Int.,* **212**(2), 1302–1313.
Whitehouse, P.L., Bentley, M.J., Milne, G.A., King, M.A. & Thomas, I.D., 2012. A new glacial isostatic adjustment model for Antarctica: calibrated and tested using observations of relative sea-level change and present-day uplift rates, *Geophys. J. Int.,* **190**(3), 1464–1482.
Wieczorek, M.A. & Meschede, M., 2018. Shtools: tools for working with spherical harmonics, *Geochem., Geophys., Geosyst.,* **19**(8), 2574–2592.
Wu, P. & Peltier, W.R., 1982. Viscous gravitational relaxation, *Geophys. J. Int.,* **70**(2), 435–485.
Wu, P., 2006. Sensitivity of relative sea levels and crustal velocities in Laurentide to radial and lateral viscosity variations in the mantle, *Geophys. J. Int.,* **165**(2), 401–413.
Wu, P., Wang, H. & Steffen, H., 2013. The role of thermal effect on mantle seismic anomalies under Laurentia and Fennoscandia from observations of Glacial Isostatic Adjustment, *Geophys. J. Int.,* **192**(1), 7–17.
Wu, X., Ray, J. & van Dam, T., 2012. Geocenter motion and its geodetic and geophysical implications, *J. Geodyn.,* **58,** 44–61.
Zhang, B. *et al.*, 2019. Geodetic and model data reveal different spatiotemporal patterns of transient mass changes over Greenland from 2007 to 2017, *Earth planet. Sci. Lett.,* **515,** 154–163.

SUPPORTING INFORMATION

Supplementary data are available at *GJI* online.

suppl_data

Please note: Oxford University Press is not responsible for the content or functionality of any supporting materials supplied by the authors. Any queries (other than missing material) should be directed to the corresponding author for the paper.

APPENDIX: IMPLEMENTATION OF NUMERICAL INTEGRATION

Considering the y_{in} system derived in Longman (1962), we can write the matricial equivalent

$$\frac{\mathrm{d}Y}{\mathrm{d}r} = S(r, \omega)Y(r), \tag{A1}$$

where $Y(r)$ is a 6 vector containing the y_i and $S(r, \omega)$ is a 6×6 matrix depending on the density ρ_0, the downward gravity field g_0, the Lamé parameters λ and μ and the radius r for a stratified Earth. Different Earth models can be used (making sure that they are spherically symmetric elastic and isotropic) like PREM (Dziewonski & Anderson 1981) or STW105 also known as REF (Kustowski *et al*. 2008). Such models are generally computed from seismological data. Several other models exist and can also be used as shown in Na & Baek (2011), especially refined crust models such as CRUST1.0 (Laske *et al*. 2013). Note that for simplest stratified cases, we can find analytical solutions using power series decomposition (Wu & Peltier 1982; Greff-Lefftz *et al*. 2005).

A1 Centre boundary conditions

In the centre of the Earth, we write that there are no displacements and the perturbed potential is null : $y_1(0) = 0, y_3(0) = 0, y_5(0) = 0$. There are consequently only three independent normalized initial conditions noted Y_A^0, Y_B^0 and Y_C^0 to propagate from $r = 0$ until the ICB (inner core boundary) using the solid system (A1)

$$\begin{cases} Y_A^0 = (0, 1, 0, 0, 0, 0) \\ Y_B^0 = (0, 0, 0, 1, 0, 0) \\ Y_C^0 = (0, 0, 0, 0, 0, 1) \end{cases}. \tag{A2}$$

The global solution at the centre is $Y(r=0) = AY_A^0 + BY_B^0 + CY_C^0$ where A, B, C are undetermined constants. All the y_i being continuous through solid–solid interface, we can perform the integration of each $Y_{A,B,C}^0$ straight to the ICB where the respective solutions are noted $Y_{A,B,C}^{\rm ICB}$. Then, we need to precisely determine the continuity of the y_i through solid–liquid interface and integrate the solution in the liquid Core.

A2 Liquid core

The equations of propagation in a liquid core are given in Chinnery (1975) for $n \geq 1$

$$\begin{cases} z_1 = \dfrac{z_5}{g_0} \\ \dot{z}_5 = z_6 + \dfrac{4\pi\mathcal{G}\rho_0}{g_0} z_5 \\ \dot{z}_6 = \left[-\dfrac{2}{r} - \dfrac{4\pi\mathcal{G}\rho_0}{g_0}\right] z_6 + \left[-\dfrac{16\pi\mathcal{G}\rho_0}{r g_0} + \dfrac{n(n+1)}{r^2}\right] z_5 \end{cases}, \tag{A3}$$

where z_i are the $n^{\rm th}$ zonal harmonic of the deformation ($i=1$), of the gravitational potential ($i=5$) and such that $z_6 = \dot{z}_5 - 4\pi\mathcal{G}\rho_0 z_1$, defined in the same way than y_6 for the solid system. We use the letter z to emphasize the conceptual difference between these variables and the one used for solid material. All the new variables are continuous throughout a liquid–liquid interface which is convenient in a stratified core. In the other hand, the solid–liquid interface conditions are (at the ICB for example) :

$$\begin{cases} y_1^{\rm ICB} = Ay_1^A + By_1^B + Cy_1^C = z_1^{\rm ICB} + K_1 \\ y_2^{\rm ICB} = Ay_2^A + By_2^B + Cy_2^C = K_1\rho_0^{\rm ICB} g_0^{\rm ICB} \\ y_3^{\rm ICB} = Ay_3^A + By_3^B + Cy_3^C = K_2 \\ y_4^{\rm ICB} = Ay_4^A + By_4^B + Cy_4^C = 0 \\ y_5^{\rm ICB} = Ay_5^A + By_5^B + Cy_5^C = z_5^{\rm ICB} \\ y_6^{\rm ICB} = Ay_6^A + By_6^B + Cy_6^C = z_6^{\rm ICB} - 4\pi\mathcal{G}K_1\rho_0^{\rm ICB} \end{cases}, \tag{A4}$$

where K_1 and K_2 are undetermined constants, $\rho_0^{\rm ICB}$ the density at the ICB in the liquid (the density should be discontinuous at the interface) and $g_0^{\rm ICB}$ the downward gravity field (continuous at the interface). Since z_1 and z_5 are linked by eqs (A3), we only need to find the expression of $z_5^{\rm ICB}$ and $z_6^{\rm ICB}$ to fully determine the initial condition of the integration in the fluid. Combining eqs (A4), we find

$$\begin{cases} z_5^{\rm ICB} = A\left[y_5^A + k_1 y_5^B + (k_2 + k_1 k_3) y_5^C\right] \\ z_6^{\rm ICB} = A\left(\left[y_6^A + k_1 y_6^B + (k_2 + k_1 k_3) y_6^C\right] + \dfrac{4\pi\mathcal{G}}{g_0^{\rm ICB}}\left[y_2^A + k_1 y_2^B + (k_2 + k_1 k_3) y_2^C\right]\right) \end{cases}. \tag{A5}$$

with undetermined constant A and where k_1, k_2 and k_3 are constants given by

$$\begin{aligned} k_1 &= \frac{\rho_0^{\rm ICB}\left(y_5^A + k_2 y_5^C\right) + \left(y_2^A + k_2 y_2^C\right) - g_0^{\rm ICB}\rho_0^{\rm ICB}\left(y_1^A + k_2 y_1^C\right)}{\rho_0^{\rm ICB}\left(y_5^B + k_3 y_5^C\right) + \left(y_2^B + k_3 y_2^C\right) - g_0^{\rm ICB}\rho_0^{\rm ICB}\left(y_1^B + k_3 y_1^C\right)}, \\ k_2 &= \frac{y_4^A}{y_4^C}, \\ k_3 &= \frac{y_4^B}{y_4^C}. \end{aligned} \tag{A6}$$

From the normalized initial conditions $\left(z_5^{\rm ICB}/A, z_6^{\rm ICB}/A\right)$, we integrate the system (A3) until the CMB (core–mantle boundary), and apply again the liquid–solid conditions (A4) to the system $\left(z_1^{\rm CMB}, z_5^{\rm CMB}, z_6^{\rm CMB}\right)$, giving

$$\begin{pmatrix} y_1^{\rm CMB} \\ y_2^{\rm CMB} \\ y_3^{\rm CMB} \\ y_4^{\rm CMB} \\ y_5^{\rm CMB} \\ y_6^{\rm CMB} \end{pmatrix} = L_1 \underbrace{\begin{pmatrix} 1 \\ g_0^{\rm CMB}\rho_0^{\rm CMB} \\ 0 \\ 0 \\ 0 \\ -4\pi\mathcal{G}\rho_0^{\rm CMB} \end{pmatrix}}_{\alpha} + L_2 \underbrace{\begin{pmatrix} 0 \\ 0 \\ 1 \\ 0 \\ 0 \\ 0 \end{pmatrix}}_{\beta} + \frac{1}{A} \underbrace{\begin{pmatrix} z_1^{\rm CMB} \\ 0 \\ 0 \\ 0 \\ z_5^{\rm CMB} \\ z_6^{\rm CMB} \end{pmatrix}}_{\gamma} \tag{A7}$$

where L_1 and L_2 are similar constants than K_1 and K_2 at the ICB and $\rho_0^{\rm CMB}$ is the density in the liquid core at the CMB.

A3 Integration until the outer surface

We then integrate the solid system (A1) through the mantle and the crust for the three independent initial conditions (α, β, γ). To obtain the global solutions, we need to determine the three constants $1/A$, L_1 and L_2 with the boundary conditions at the outer surface which are

described in Section 3.1. The 6 unknown at the outer surface $[y_1(a), y_3(a), y_5(a), 1/A, L_1, L_2]$ can be obtained by solving the following Cramer system with a right member vector containing the outer boundary conditions

$$\begin{pmatrix} y_1^\alpha & y_1^\beta & y_1^\gamma & -1 & 0 & 0 \\ y_2^\alpha & y_2^\beta & y_2^\gamma & 0 & 0 & 0 \\ y_3^\alpha & y_3^\beta & y_3^\gamma & 0 & -1 & 0 \\ y_4^\alpha & y_4^\beta & y_4^\gamma & 0 & 0 & 0 \\ y_5^\alpha & y_5^\beta & y_5^\gamma & 0 & 0 & -1 \\ y_6^\alpha & y_6^\beta & y_6^\gamma & 0 & 0 & \dfrac{n+1}{a} \end{pmatrix} \begin{pmatrix} L_1 \\ L_2 \\ 1/A \\ y_1(a) \\ y_3(a) \\ y_5(a) \end{pmatrix} = \begin{pmatrix} 0 \\ -\left(\dfrac{(2n+1)g_e}{4\pi \mathcal{G}a} U_n' + P_n\right) \\ 0 \\ \tau_n \\ 0 \\ \dfrac{2n+1}{a}(U_n + U_n') \end{pmatrix}. \tag{A8}$$

We note that the boundary conditions in the outer surface (eq. 10) are applicable only if the outer layer of the Earth is solid. In the case of PREM, the outer layer is the ocean and is therefore liquid. Then it is common to replace this ocean layer by an extension of the last crustal layer. If we do this, we actually increase the density of the outer layer such that the mass of the Earth is a little larger than in the original PREM. In order to keep the original value for the mass of the Earth, we need to reassign the density of the outer crust layer as the average of the density of the ocean and the crust, weighted by the corresponding thickness of these two layers. Finally, we found an average density of 2283.4 kg·m^{-3} which is less than the original density 2600 kg·m^{-3} of the top crust layer. The difference in the Love numbers can be important especially in the high degrees asymptote. This difference reaches 15 per cent for k' (h' and l' are not affected) and between 15 per cent and 45 per cent for the TLN. We choose here to replace the ocean by the crust using the modified value of the density as Martens *et al*. (2016) did.

A4 Remarks on numerical integration

A4.1 Integration in $r = 0$

The gravito-elastic system (A1) is not mathematically defined at the origin. There are two options in order to perform the integration. The first is to begin the integration of the system from a small non-zero radius (for example $R = 1$ km) to avoid the singularity. The second is to consider an homogeneous sphere of same radius R and determine the analytical solution of the homogeneous problem inside (Greff-Lefftz *et al*. 2005). This gives three independent solutions multiple of three constants A, B and C which are the initial conditions of the numerical integration replacing the conditions (A2). These two methods give similar results for degrees beyond 1 especially for small radii ($R < 10$ km).

A4.2 High degree integration

It is common to implement a dimensionless form of the system for computational convenience. The equations and the boundary conditions at the surface are then divided by dimensional constants (Longman 1963). The major advantage is to perform the integration for high degrees without numerical divergence issues. We used a Runge–Kutta integrator of order 2 with integration step as small as needed and a normalization of the integration result (result is between -1 and 1). Of course, the constants $1/A$, L_1 and L_2 are affected but there are no consequences in the surface Love numbers as they are determined simultaneously to the three constants in the inversion of (A8). However, the integration function to compute Love numbers in the deep interior presented in Section 5.2 have to be unnormalized since the constants are used to determine the solutions in depth. For degrees $n > 300$, the Love numbers are no longer dependent in the inner core and liquid core structure and we can perform the integration from the base of the mantle (at the CMB) as if we integrate from the centre, applying the initial conditions (A2). The difference between a mantle and total integration for these degrees are around numerical errors ($\sim 10^{-8}$ in relative values).